

Multiscale Analysis of the Summertime Precipitation over the Central Andes

RENÉ D. GARREAUD*

Department of Atmospheric Sciences, University of Washington, Seattle, Washington

(Manuscript received 8 February 1998, in final form 28 May 1998)

ABSTRACT

Precipitation over the central Andes in South America exhibits a marked annual march, with most of the rainfall concentrated during the austral summer season (December–February), when the atmospheric circulation favors the uplifting of moist air from the lowlands to the east of the mountain range. Within its rainy season, the central Andes experiences week-long rainy and dry episodes. The large-scale and local conditions during these episodes are investigated using satellite imagery, reanalyzed atmospheric fields, and in situ data. Despite the deep layer of conditional instability prevalent during most summertime afternoons, deep convection can occur only on those days in which the mixing ratio within the local boundary layer exceeds some threshold ($\sim 7 \text{ g kg}^{-1}$), yielding saturation of near-surface air parcels rising more than 600 m above ground. Convective cloudiness anomalies over the central Andes extend southeastward and tend to be concurrent with anomalies of opposite sign over the eastern part of the continent. Rainy (dry) episodes are also associated with anticyclonic (cyclonic) anomalies centered over subtropical South America that extend through the depth of the troposphere, accompanied by easterly (westerly) wind anomalies over the central Andes. These anomalies are presumably forced by planetary waves originating in the Southern Hemisphere extratropics.

To gain insight into the regional processes linking the large-scale and local conditions, The Pennsylvania State University–National Center for Atmospheric Research Mesoscale Model Version 5.2 was used to simulate contrasting rainy and dry episodes. The most marked and relevant differences are the strength and extent of diurnally varying flow over the eastern slope of the Andes. During the rainy simulation, strong easterly winds reach the upper part of the slope by midmorning, initiating an intrusion of warm and moist air (high θ_e air originating in the eastern lowlands) into the central Andes. In the dry case, the moisture transport from the east is restricted to the eastern slope of the Andes, and the central Andes is flooded by low θ_e air from the western foothills that cannot support deep convection even in the presence of localized updrafts. The momentum balance based on the model output indicates that turbulent momentum mixing from aloft (determined by the large-scale anomalies of the upper-level flow) into the convective boundary layer is the leading term causing the differences in the daytime upslope flow (and hence moisture transport) over the upper part of the eastern side of the Andes between rainy and dry simulations.

1. Introduction

The influence of mountains upon the intensity, position, and timing of convective rainfall is widely recognized (e.g., Banta 1991; Houze 1993). From a continental-scale perspective there is a clear enhancement of convective rainfall over or near large mountain ranges, particularly during the warm season. For instance, during the boreal summer, convection over Central America is enhanced over the western slopes of the Sierra Madre Occidental, extending northwestward along the continental divide as far as the southwestern

United States (Negri et al. 1993). Summertime convection over the Colorado Rockies propagates eastward in a significant number of cases, becoming mesoscale convective systems over the Great Plains states (e.g., Tripoli and Cotton 1989). Heavy summertime rainfall also characterizes the eastern edge of the Tibetan Plateau (Tang and Reiter 1984). During the austral summer (December–January–February, DJF), a distinctive band of deep convection is found along the central Andes in South America (Fig. 1), separate from a more extensive area of convective cloudiness over the central part of the continent (e.g., Garreaud and Wallace 1997).

The Andes range is one of the most important topographic features of South America, extending from north of the equator to the southern tip of the continent. Along its central portion (15° – 22°S) it splits into two ranges surrounding an intermountain basin, known as the Altiplano, about 250 km wide and at an average elevation of 3800 m ($\sim 620 \text{ hPa}$) (Fig. 2). To the west of the central Andes, the South Pacific subtropical anticyclone produces dry and stable conditions, with moist

* Current affiliation: Department of Geophysics, University of Chile, Santiago, Chile.

Corresponding author address: Dr. René D. Garreaud, Department of Geophysics, University of Chile, Casilla 2777, Santiago, Chile.
E-mail: rgarreau@dgf.uchile.cl

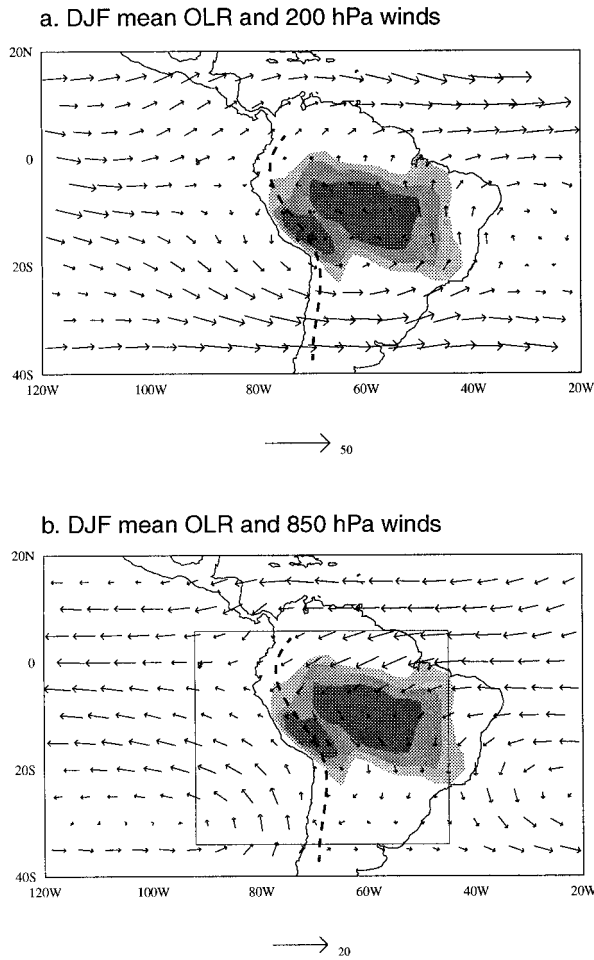


FIG. 1. (a) Austral summer (DJF) climatological mean OLR and 200-hPa winds. Light, medium, and dark shading indicate OLR values less than 230, 220, and 210 $W m^{-2}$, respectively. The thin dashed line represents the Andes mountains. (b) As in (a) but for 850-hPa winds. The open box in (b) indicates the outer domain used in the model simulation.

air confined below the base of the subsidence inversion around 900 hPa, whereas over the lowlands to the east of the Andes the low-level circulation is controlled by a heat low (e.g., Zhou and Lau 1998) and high humidities prevail in the lower and middle troposphere. This marked difference in moisture on the two sides of the central Andes is illustrated in Fig. 3, which shows the climatological profiles of water vapor mixing ratio. Situated in between these contrasting atmospheric conditions, the Altiplano exhibits distinctive climatic features described in Aceituno (1997) and summarized later in this paper.

Early studies have documented the episodic and convective nature of the rainfall over the Altiplano associated with uplifting of moist air from the lowlands to the east of the Andes (Schwerdtfeger 1976; Fuenzalida and Rutllant 1987; Aceituno and Montecinos 1993). In a study of the mean summertime precipitation over

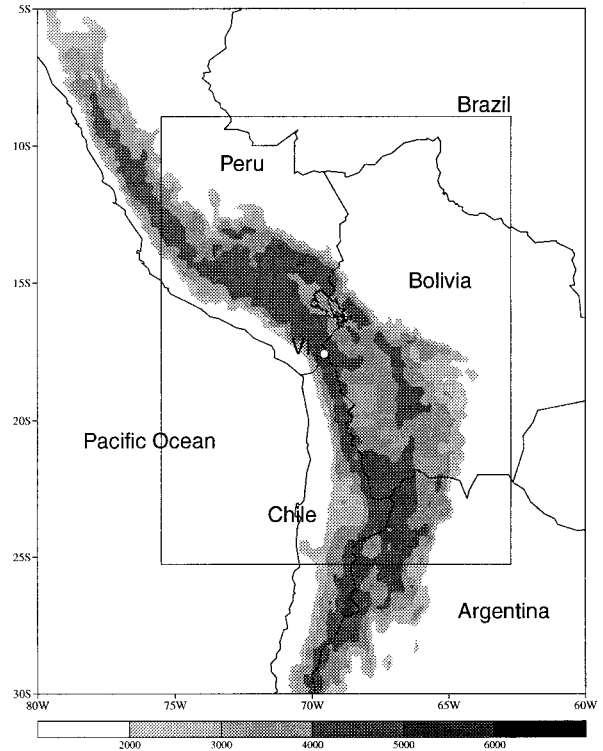


FIG. 2. Topographic map of the central Andes. Elevation scale in meters MSL. The small open circle indicates the location of Visviri. The open box indicates the inner domain used in the model simulation.

South America using a general circulation model, Lenters and Cook (1995) also found that vertical moisture flux convergence due to the local orography is the leading mechanism governing the precipitation over the Altiplano. Rao and Erdogan (1989) computed the mean atmospheric heat balance over the Altiplano using conventional surface and satellite radiation data for January 1979. Their results indicate the existence of an atmospheric heat source over most of the Altiplano, with an average heating rate of $1 K day^{-1}$ for the 700–100-hPa layer dominated by the contribution of the latent heat ($\sim 500 W m^{-2}$). More recent works have emphasized the continental-scale anomalies of convective cloudiness and the upper-level circulation during the week-long rainy and dry episodes over the Altiplano. During these episodes, a coherent band of outgoing longwave radiation (OLR) anomalies extends southeastward from the Altiplano, whereas anomalies of the opposite sign prevail over the east coast of the continent (Aceituno and Montecinos 1997a; Lenters and Cook 1999). A reinforcement and southward displacement of the climatological Bolivian high is also observed during rainy episodes (Aceituno and Montecinos 1993; Lenters and Cook 1999). In addition to these prevalent features, Lenters and Cook (1999) and Vuille et al. (1998) have documented distinctive types of circulation anomalies to the east of the Andes associated with rainy periods over the central Andes. The precipitation over the Altiplano

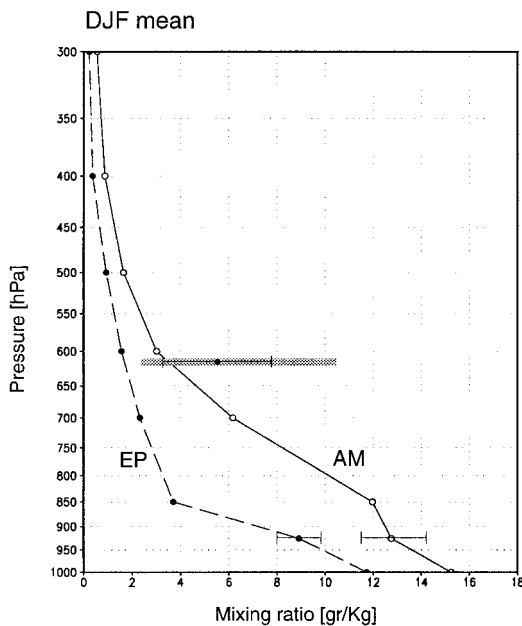


FIG. 3. Austral summer (DJF) mean profiles of mixing ratio at 20°S, 72°W (eastern Pacific, EP), and 20°S, 60°W (Amazon Basin, AM). The horizontal lines indicate ± 1 std dev of the respective profile at the corresponding level. Data are from the NCEP–NCAR reanalysis. The gray bar indicates range of variability of mixing ratio observed over Visviri and the small dot is its seasonal mean (data from Visviri I and II).

also exhibits substantial year-to-year variability, with a tendency to dry conditions during the warm phase of the El Niño–Southern Oscillation phenomenon (Thompson et al. 1984; Aceituno and Garreaud 1995). On the other side of the spectrum, our knowledge of local conditions is based mainly on two field experiments carried out on the Chilean side of the Altiplano during January of 1994 and 1995 (Aceituno et al. 1995; Aceituno and Montecinos 1997b). During both rainy and dry periods, the moisture transport is strongest during afternoon and evening and peaks near the 500-hPa level. Relatively high levels of moisture throughout the tropospheric column and a weaker-than-normal local low-level southwesterly flow capped by easterly winds in the middle troposphere tend to prevail during the rainy episodes (Aceituno and Montecinos 1997b).

The studies cited above have revealed many large-scale features and local conditions associated with the variability of the summertime rainfall over the central Andes. Yet there is a significant gap in our knowledge, especially with regard to the regional processes linking large-scale anomalies with local conditions, the latter being ultimately responsible for the occurrence of convectively active or inactive episodes. In the present study we aim to improve our understanding of the actual mechanisms responsible for the occurrence of rainy and dry episodes over the Altiplano, with emphasis on the interaction between continental-, regional-, and local-scale phenomena. First, we investigate the large-scale

patterns and local conditions during the rainy and dry episodes using gridded fields of the relevant meteorological variables, satellite observations of convective cloudiness, and surface data. Second, we analyze the regional processes using a mesoscale numerical model to simulate a pair of dry and rainy episodes with the hope that the model output would provide a physically consistent, high-resolution dataset. Here regional scale connotes meso- α scale—that is, horizontal distances range from 200 to 2000 km (Orlanski 1975). The paper is structured as follows. A description of the datasets is given in section 2. Section 3 discusses the climatological background, with emphasis on the annual and diurnal cycles over the central Andes. Analyses of the local and large-scale conditions during rainy and dry episodes are presented in section 4. Section 5 describes the mesoscale numerical model and simulation strategy, followed by the relevant model results. Finally, in the conclusions we merge our local and large-scale observations with the regional model results to form a conceptual model of the functioning of rainy and dry episodes over the central Andes.

2. Datasets

Four datasets have been used in the observational part of this study. The National Centers for Environmental Prediction–National Center for Atmospheric Research (NCEP–NCAR) reanalyzed meteorological fields described in detail in Kalnay et al. (1996) are used to characterize the large-scale tropospheric circulation and thermodynamic structure.¹ The original fields have 6-h resolution on a 2.5° latitude–longitude grid and include all mandatory levels from 1000 to 100 hPa (300 hPa for humidity). The 1200 and 2400 UTC data (0800 and 2000 LST at 60°W) were merged to produce daily fields during the austral summer months (DJF) from 1979 to 1995. The second dataset consists of daytime and nighttime fields of outgoing longwave radiation with a 2.5° latitude \times 2.5° longitude resolution, measured by polar-orbiting satellites and produced by National Oceanic and Atmospheric Administration (NOAA)–NCEP (Gruber and Krueger 1984). For the same period of record we averaged the twice-daily OLR observations and defined a convective index (CI) as 230 OLR if OLR < 230 $W m^{-2}$ or 0 otherwise. The threshold 230 $W m^{-2}$, which

¹ An important caveat in the use of the NCEP–NCAR reanalysis over the Southern Hemisphere is the use of incorrectly assimilated (shifted by 180° longitude) Australian surface pressure bogus data (PAOBs) between 1979 and 1992. The impact of the PAOBs' mislocation in the present analyses should be small since the area of interest is mainly over subtropical and tropical South America, where in situ data strongly damp any error propagating from the southern Pacific Ocean. Any remaining errors should be random relative to the timing of the wet and dry episodes over the Altiplano and therefore it is difficult to see how they could be responsible for the dynamically coherent structures revealed by the analysis in section 4.

corresponds to a cloud-top temperature of about 250 K, is low enough to filter out variations in ground temperature and low-level cloudiness.

For a more detailed analysis of the convective cloudiness over the central Andes, we have used 11 years (1983–93) of reduced resolution radiance images [the B3 International Satellite Cloud Climatology Project (ISCCP) product] from geostationary satellites *GOES-5*, *-6*, and *-7*. The B3 dataset is a compressed version of the original GOES images to a nominal resolution of 30 km every 3 h (eight images per day beginning at 0000 UTC). Further details of this dataset are given in Rossow and Schiffer (1991). In this study we converted the 3-hourly pixel maps of infrared radiance ($11.6 \mu\text{m}$) to a regular 0.5° latitude \times 0.5° longitude grid of brightness temperature (T_b), following the procedure described in Garreaud and Wallace (1997).

In situ meteorological observations over the Altiplano were obtained from two field experiments conducted in the small town of Visviri [17.5°S , 69.5°W , 4070 m above mean sea level (MSL), see Fig. 2] and described in Aceituno et al. (1995) and Aceituno and Montecinos (1997b). The field experiments Visviri I and II were carried out during 19–29 January 1994 and 11–22 January 1995. They included four daily rawinsoundings (20-hPa vertical resolution) and near-surface hourly observations of solar radiation, air temperature, humidity, wind, and precipitation (Aceituno and Montecinos 1997b). In addition to the field experiments, near-surface meteorological data were continuously collected by an automatic weather station maintained at Visviri from October 1993 to November 1995 (Aceituno and Montecinos 1997b). Comparison between daily mean mixing ratio at Visviri and its corresponding daily reanalysis value at 17.5°S , 70°W , interpolated at 620 hPa, reveals a reasonable correlation between local and reanalysis data ($r = 0.55$) and similar ranges of day-to-day variability ($2\text{--}8 \text{ g kg}^{-1}$) of both measurements during the two austral summers with available local data.

3. Background: Annual and diurnal cycles

Precipitation over the Altiplano exhibits a pronounced annual cycle, with more than 70% of the rain concentrated in the austral summer (Aceituno and Montecinos 1993), associated with the development of convective cloudiness over the central Andes and the southwestern part of the Amazon Basin (Horel et al. 1989, see also Fig. 1). Area-average rainfall is about 220 mm per year (Legates and Willmont 1990), although there is a significant gradient, with higher rainfall in the northeastern part of the Altiplano, characterized by the presence of the basin of Lake Titicaca, and substantially drier conditions in the southwestern part of the plateau, manifest in the existence of extensive dry lakes (Aceituno 1997).

The specific humidity and zonal wind over the Altiplano also exhibit a marked annual march, with the

highest humidity in January in association with weak easterly flow in the middle and upper troposphere and the minimum OLR. In contrast, the annual marches of solar radiation and surface maximum air temperature (not shown) are relatively small, both experiencing a weak maximum in November, just before the onset of the rainy season (Aceituno 1997). The large-scale mean summertime flow at upper levels exhibits a broad anticyclone centered just to the east of the central Andes (the so-called Bolivian High, Fig. 1a) first identified by Gutman and Schwerdtfeger (1965) and Virji (1981) and linked to the strong diabatic heating over the Amazonia in subsequent modeling studies (e.g., Figueroa et al. 1995; Lenters and Cook 1997). At lower levels (Fig. 1b), the barrier effect of the Andes is clear, separating the northwesterly flow over the western half of the Amazon Basin and the subtropical plains of the continent from the southeasterly flow over the eastern Pacific.

Consistent with its latitude and elevation, near-surface conditions over the Altiplano are strongly coupled to insolation and exhibit a pronounced diurnal cycle. During summer, maximum surface air temperature of about 12°C typically occurs shortly after midday, whereas below freezing temperatures prevail between midnight and dawn. Strong fluxes of sensible heat during morning and afternoon [$Q_h \sim 600 \text{ W m}^{-2}$ at midday (H. Fuenzalida 1997, personal communication)] build up a deep, well-mixed boundary layer that reaches a maximum vertical extent of about 1800 m around 1600 LST, whereas longwave cooling and weak winds favor the formation of very stable nocturnal stratification. Coupled to the daytime destabilization of the (local) lower troposphere, convective cloudiness over the central Andes reaches a late afternoon maximum, characterized by deep elongated cells ($T_b < 205 \text{ K}$) embedded in a more extensive shield of moderately cold cloudiness. The late afternoon maximum of convective cloudiness (defined by $T_b < 235 \text{ K}$) is preceded by a rapid buildup phase between 1200 and 1600 LST, a more gentle decay during nighttime, and an early morning minimum (Garreaud and Wallace 1997). The rainfall over the Altiplano exhibits a similar diurnal cycle, with most of the precipitation produced by thundershowers between 1700 and 2200 LST (Aceituno 1998).

4. Rainy and dry episodes over the Altiplano

Within its rainy season, the Altiplano experiences rainy and dry episodes with durations ranging between 5 and 10 days (Fuenzalida and Rutllant 1987; Aceituno and Montecinos 1993). Indirect evidence of this episodic character is given in Fig. 4, which shows the fraction of Altiplano area covered by convective cloudiness (ACC) during the evening (1800 LST) for two summers. In this estimation the Altiplano is defined as the region with terrain elevation in excess of 3400 m MSL between 16° and 22°S . In spite of the day-to-day variability, there is evidence of alternating, week-long periods of high

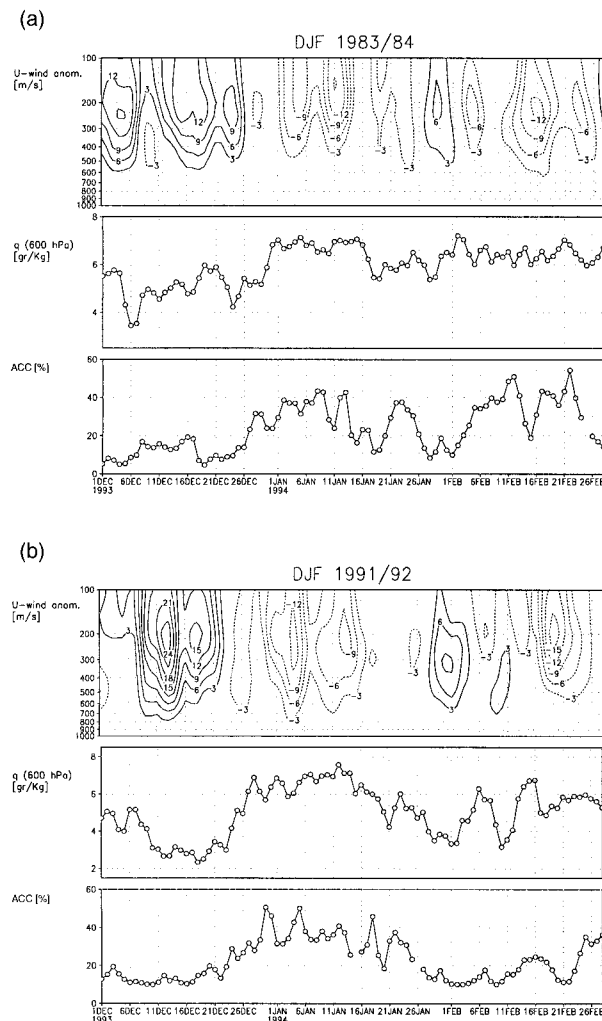


FIG. 4. (a) Daily time series of zonal wind anomalies (upper panel, negative values indicated by dashed lines) and specific humidity at 600 hPa (middle panel) over the central Andes (15° – 21° S, 71° – 66° W), and fraction of the Altiplanic area cover by convective cloudiness ($T_b < 235$ K) from 1 December 1983 to 28 February 1984. (b) As in (a) but for the austral summer of 1991–92. Zonal wind and specific humidity from NCEP–NCAR reanalysis. Convective cloudiness calculated from the B3 ISCCP dataset (0.5° lat \times 0.5° long resolution).

and low convective cloudiness coverage, indicative of relatively wet and dry conditions, respectively. For example, the summer of 1983–84 was characterized by three “rainy” periods (ACC > 30%) from the end of December to mid-January, early and late February, separated by extended periods when ACC was consistently less than 10%. In the summer of 1991–92 the outstanding rainy periods encompass late December, most of January, and late February. Figure 4 also includes reanalyzed daily values of the mixing ratio at 600 hPa and zonal wind anomalies averaged over the Altiplano region. These diagrams suggest the simultaneous occurrence of rainy periods, high water vapor content, and easterly wind anomalies in the middle and upper tro-

posphere, and vice versa, in concurrence with previous findings of Fuenzalida and Rutllant (1987) and Aceituno and Montecinos (1993).

a. Large-scale patterns

Summertime episodes of active and suppressed convection over the Altiplano were objectively selected between 1979 and 1995, on the basis of the average CI over a $2.5^{\circ} \times 2.5^{\circ}$ box centered at 18° S, 69° W. Using a smoother² version (CI*) rainy (dry) episodes were defined as continuous sequences of at least four days in which CI* was equal to or larger (less) than the seasonal mean plus (minus) 0.6 standard deviations. The factor 0.6 is arbitrary and was chosen so as to select at least two rainy periods per summer. With this criterion, 36 rainy and 43 dry episodes were selected out of the 15 austral summers, with average durations of 6.8 and 10.3 days, respectively. Although in each summer only half of the days are classified as belonging to one of two categories, rainy and dry episodes are still of practical relevance owing to the long-lasting anomalies that they represent. Based on this pool of episodes we made a compositing analysis of CI, several meteorological fields, and brightness temperature with the aim of characterizing the large-scale conditions during the rainy and dry episodes over the Altiplano. Composite anomalies were calculated as the difference between the composite maps and their respective seasonal mean.

Figures 5a and 6a show the CI anomalies during rainy and dry composites. Consistent with the definition of the composite, the largest anomalies are centered along the central Andes, between 15° and 25° S, and encompass the westernmost part of Amazonia. In both composites, significant anomalies of opposite sign to the Andean ones are found over southeast Brazil, forming a dipolar, continental-scale pattern of convective anomalies in the southern half of the area of intense convection over the continent (Fig. 1a). The tendency for out-of-phase anomalies of convective cloudiness and precipitation between the east coast–South Atlantic convergence zone domain and the subtropical plains–central Andes on weekly or longer timescales has also been reported by Nogues-Paegle and Mo (1997), Aceituno and Montecinos (1997a), and Lenters and Cook (1999). Differences in convective cloudiness over the Altiplano during rainy and dry episodes are further illustrated in Fig. 7 by means of the diurnal march of the fractional area covered by convective cloudiness derived from the B3 ISCCP data (in this case the composites are calculated using previously selected episodes between 1983 and 1993). About 50% of the Altiplano is covered by cold clouds ($T_b < 235$ K) during the afternoons of rainy

² For each grid point, CI* at day j is calculated as $CI^*(j) = [CI(j-1) + 2CI(j) + CI(j+1)]/4$.

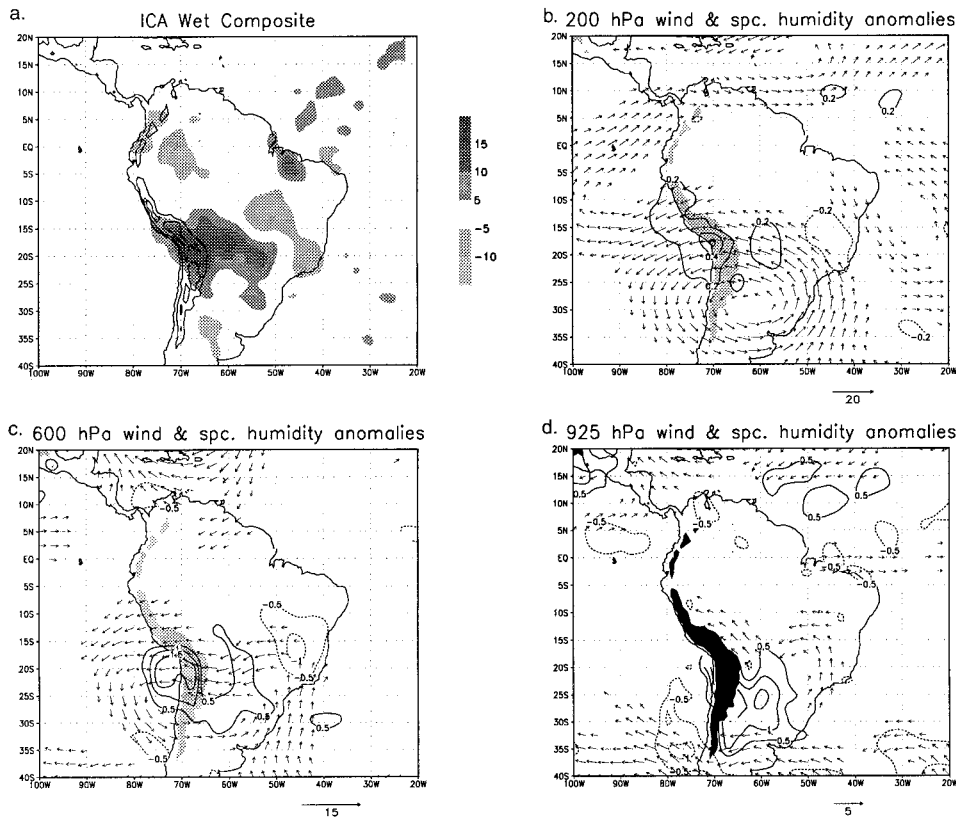


FIG. 5. (a) Convective index anomalies for the wet composite ($W m^{-2}$). The 2000- and 4000-m topographic contours are indicated by solid lines. (b) 200-hPa wind anomaly ($m s^{-1}$) and 300-hPa specific humidity anomalies ($g kg^{-1}$) for the wet composite. Anomalies are calculated as the composite mean minus the climatological mean. Only wind anomalies locally statistically significant at the 95% confidence level are shown. The 2000-m topographic contour is indicated by a solid line. (c) As in (b) but at 600 hPa. Mixing ratio anomalies in excess of $\pm 0.6 g kg^{-1}$ are statistically significant at 95% confidence level. (d) As in (b) but at 925 hPa. Mixing ratio anomalies in excess of $\pm 0.9 g kg^{-1}$ are statistically significant at the 95% confidence level. The shaded/black area indicates terrain elevations in excess of 2000 m. Analysis based on data from 1979 to 1995. Confidence levels based on a two-sided Student's *t*-test, assuming a decorrelation time of five days for estimating number of degrees of freedom.

episodes, while convective cloudiness is almost non-existent during dry episodes. Rainy episodes also are characterized by a significant amount of cold clouds over the Altiplano during the first half of the nighttime period. Figures 5 and 6 also show the horizontal wind and specific humidity anomalies at 200, 600, and 900 hPa. In the rainy composite, a broad anticyclonic anomaly at upper levels (200 hPa, Fig. 5b) is centered at 25°S, 60°W, strengthening and shifting southward the climatological Bolivian high and reinforcing the westerly flow south of 35°S (Fig. 1a). The geopotential anomalies exhibit an equivalent barotropic structure (a warm core anticyclone), and therefore easterly wind anomalies (weak easterly flow) prevail at and above the crest of the central Andes (600 hPa, Fig. 5c). The stronger-than-normal upper-level easterly flow is a common ingredient in the different patterns associated with summertime precipitation over the Altiplano reported by Lenters and Cook (1999) and Vuille et al. (1998). In the upper and middle troposphere the spe-

cific humidity exhibits small positive departures over the central Andes and the eastern Pacific, which is consistent with the easterly zonal flow anomalies. At lower levels, the anticyclonic anomalies are distorted by the Andes, but the anomalous easterly flow over much of the central part of the continent is still evident. Roughly the opposite situation prevails in the dry composite (Fig. 6), with continental-scale circulation anomalies dominated by a cold core cyclone centered at 25°S, 60°W, and the central Andes exposed to westerly wind anomalies (weak westerly flow) (Figs. 6b,c). Weak westerly wind anomalies are observed over the lowlands near the eastern slope of the Andes in this case (Fig. 6d). Also note that for both composites, mixing ratio anomalies (reanalysis data) in the lower troposphere (925 hPa) to the east of the central Andes are too small ($\pm 0.5 g kg^{-1}$) to account for the moisture variability over the Altiplano ($\pm 1.5 g kg^{-1}$) (Figs. 5c,d and 6c,d).

The large-scale upper- and midlevel circulation pat-

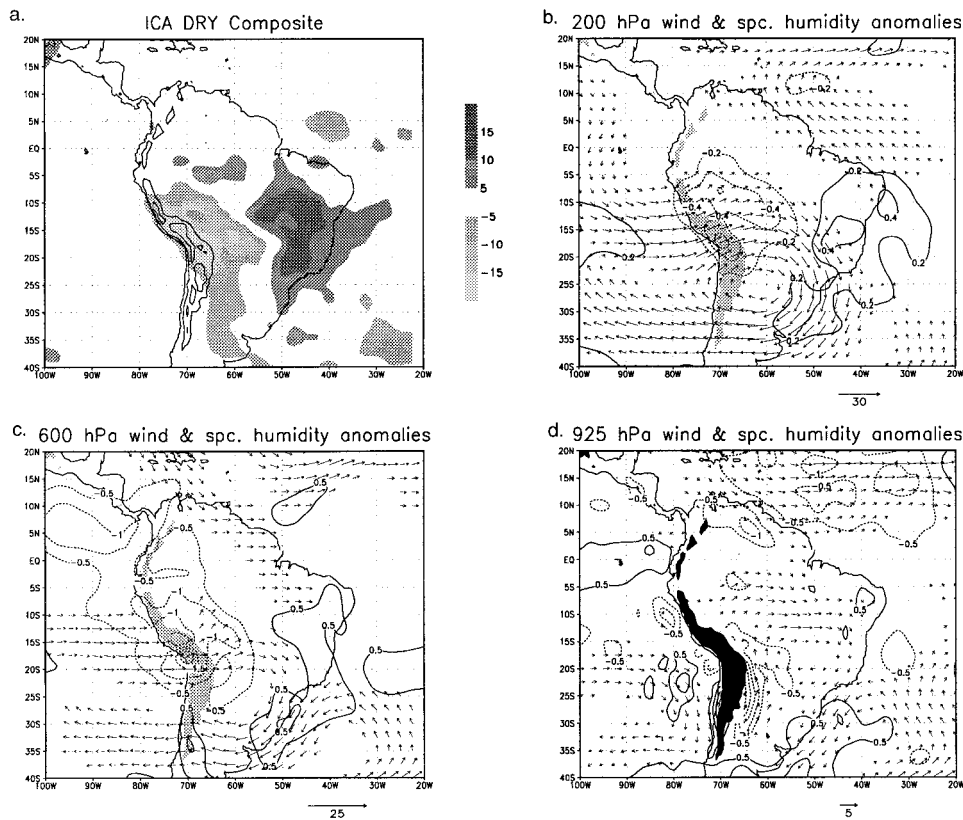


FIG. 6. As in Fig. 5 but for the dry composite.

terns that emerge from the compositing analysis are statistically robust, consistent with previous findings referred to in the introduction, and also captured by a singular value decomposition analysis between 300 hPa winds and CI (not shown). Their equivalent barotropic structure and position to the east of the central Andes suggest that large-scale circulation anomalies are not directly forced by the anomalous heat source, but rather that they lead to the convective anomalies over the Al-

tiplano. A likely source of these subtropical height departures on weekly timescales is Rossby wave dispersion from the Southern Hemisphere extratropics in the upper-level westerly ducts that extend into the Tropics (e.g., Kiladis and Weickmann 1997). In support of this hypothesis, Fig. 8 shows the correlation coefficient between the 200-hPa geopotential height at 27°S, 60°W (i.e., the center point of the anomalies in the composite) and geopotential height at every grid point at 200, 500,

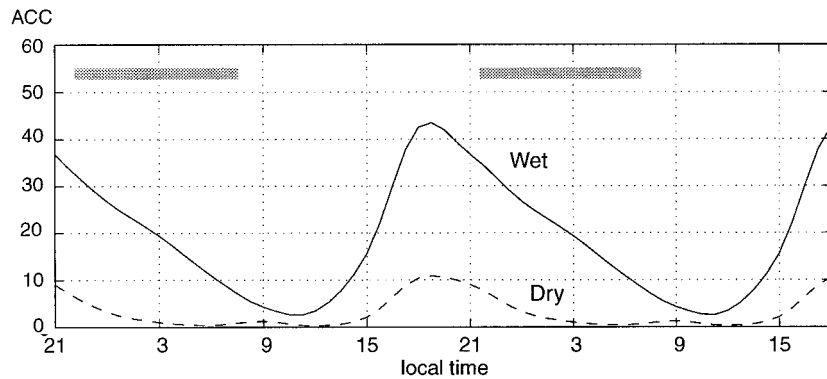


FIG. 7. Diurnal cycle of the fraction (percent) of the central Andes area (15°–21°S, 71°–66°W) covered by convective cloudiness ($T_b < 235$ K) for the wet composite (solid line) and dry composite (dashed line). The diurnal cycle is repeated twice. Gray bars at the top indicate nighttime. Data are from B3 ISCCP (1983–93).

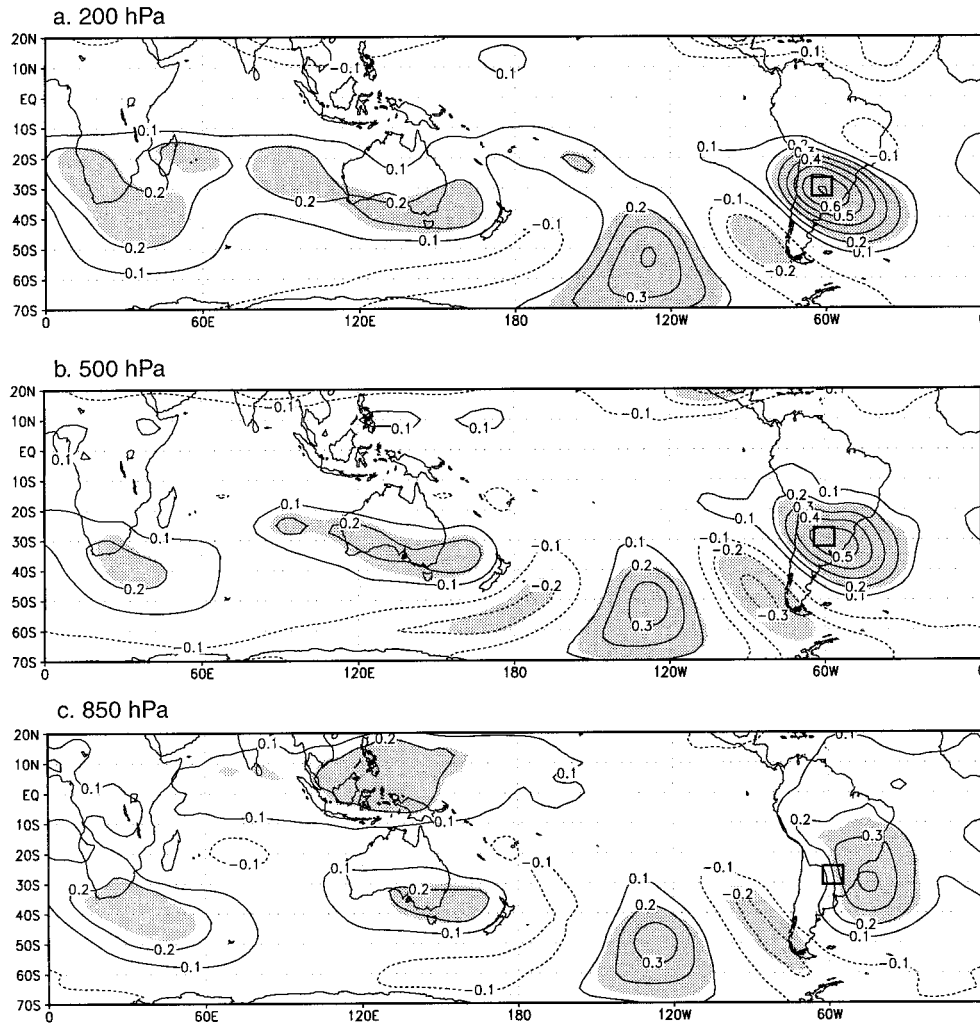


FIG. 8. Correlation coefficient between low-pass filtered 200-hPa geopotential height over a grid box centered at 25°S, 57.5°W (indicated by an open square over subtropical South America) and (a) low-pass filtered 200-hPa geopotential height at every grid point, (b) low-pass filtered 500-hPa geopotential height at every grid point, and (c) low-pass filtered 850-hPa geopotential height at every grid point. Contour interval is 0.1, negative values are indicated by dashed lines, and the zero contour is omitted. Light shading indicates the 95% significance level (based on a two-sided Student's *t* test, assuming a decorrelation time of 5 days for estimating number of degrees of freedom).

and 850 hPa. The time series were low-pass filtered to retain fluctuations with periods longer than five days only. Connected with the local equivalent barotropic anomalies there is a signature of a wave train with a wavelength of 70° longitude that extends from the South Pacific, amplifies downstream over subtropical South America, and agrees with a similar analysis reported by Jones (1990). Although this pattern may be forced by random, longitude-independent planetary waves, its similarity to the leading modes of the Southern Hemisphere circulation anomalies (e.g., Mo and Higgins 1997), referred to as the Pacific South American mode and linked to intra-seasonal fluctuations in convection over the western Pacific–Indian Ocean region, is noteworthy.

b. Local conditions

Insights into the local thermodynamic conditions during rainy and dry episodes are obtained from the upper-air observations during Visviri I and II. Our previous selection of episodes based on CI* (section 4a) was complemented with local weather observations and rainfall records to define rainy (active convection) and dry (suppressed convection) days over the western Altiplano. For the two experiments, Fig. 9 shows time-pressure sections of the difference ($\delta\theta_e$) between near-surface equivalent potential temperature, θ_e (600 hPa), and the ambient saturated equivalent potential temperature, $\theta_e^*(p)$. At any given time, $\delta\theta_e > 0$ at level p^* indicates

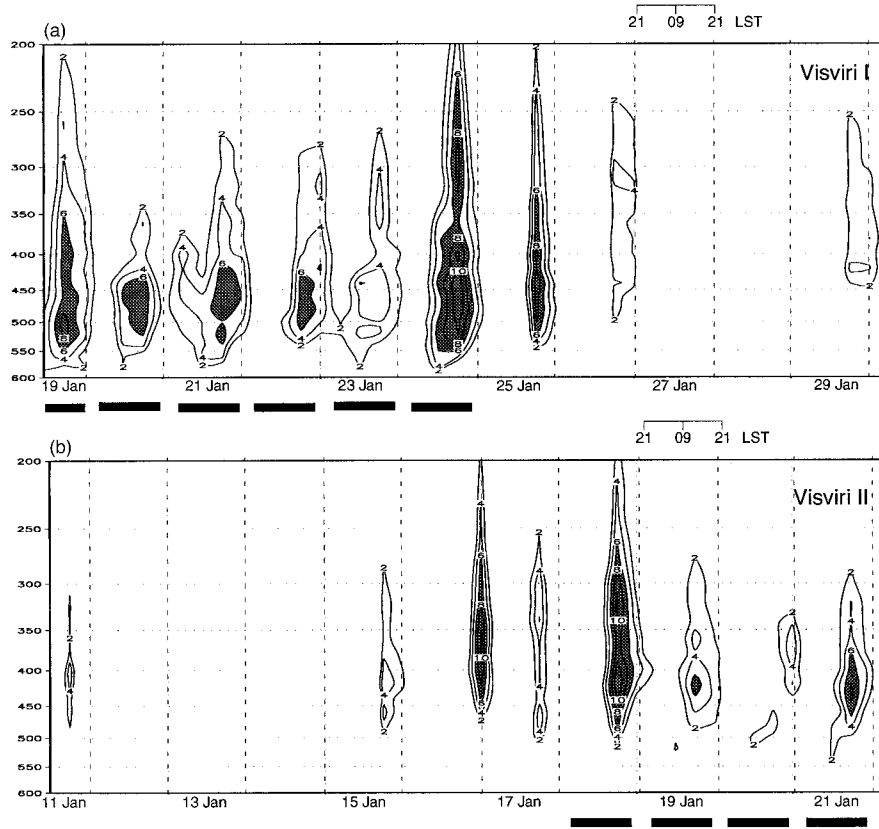


FIG. 9. Time–pressure sections of the difference between the equivalent potential temperature at 600 hPa and the saturated equivalent potential temperature throughout the tropospheric column ($\theta_e^* - \theta_{e(600 \text{ hPa})}$). Contours begin at +2 K, the contour interval is 2 K, and values in excess of 6 K are shaded. The diagrams were constructed using the four times daily soundings taken during (a) Visviri I and (b) Visviri II. Days with active convection are indicated by a black bar at the bottom.

that an air parcel lifted from the surface to p^* has become saturated and positively buoyant (Holton 1992); the lower and upper limits of the region with $\delta\theta_e > 0$ are the level of free convection (LFC) and level of neutral buoyancy (LNB), respectively; and the integral of $\delta\theta_e$ between LFC and LNB (if such a layer exists) is proportional to the convective available potential energy (CAPE). Active convection over Visviri (highlighted in Fig. 9) occurred almost exclusively on those days with nonzero CAPE afternoon soundings: the first half of Visviri I and the final days of Visviri II. Also evident is the diurnal cycle of the local troposphere thermodynamic destabilization, with conditionally unstable conditions ($\delta\theta_e > 0$) mainly confined between afternoon and early night.

Composite afternoon (1500 LST) soundings for rainy (active convection) and dry (inactive convection) days during Visviri I and II are shown in Fig. 10. Both soundings exhibit a conditionally unstable layer ($\partial\theta_e^*/\partial z < 0$) from the surface to 400 hPa. However, the release of conditional instability (near-surface θ_e equal to θ_e^* at some level) may happen only in the active case when LFC \sim 550 hPa, LNB \sim 200 hPa, and CAPE \sim 500

J kg^{-1} . The key factor in producing a nonzero CAPE is the higher θ_e near the surface during the active days, although the observed midtropospheric cooling also contributes to increase the available potential energy. Consistent with a slightly cooler troposphere and reduced surface insolation under active convection conditions, the air temperature within the mixed layer is 2–3 K lower during active days. Therefore, the higher θ_e near the surface is entirely produced by a higher ($\sim 4 \text{ g kg}^{-1}$) mixing ratio near the surface (q_{LL}) during active days. Furthermore, the mean values of q_{LL} (using the observations taken at Visviri) for dry and rainy episodes (selected on the basis of CI*) during the summers 1993–94 and 1994–95 are 3.5 ± 0.7 and $6.8 \pm 0.9 \text{ g kg}^{-1}$, respectively. These values indicate a marked difference in the near-surface moisture content at Visviri between rainy and dry episodes over the Altiplano.

5. Regional processes

a. Model description and simulation strategy

In this section we describe results obtained using The Pennsylvania State University–NCAR Mesoscale Mod-

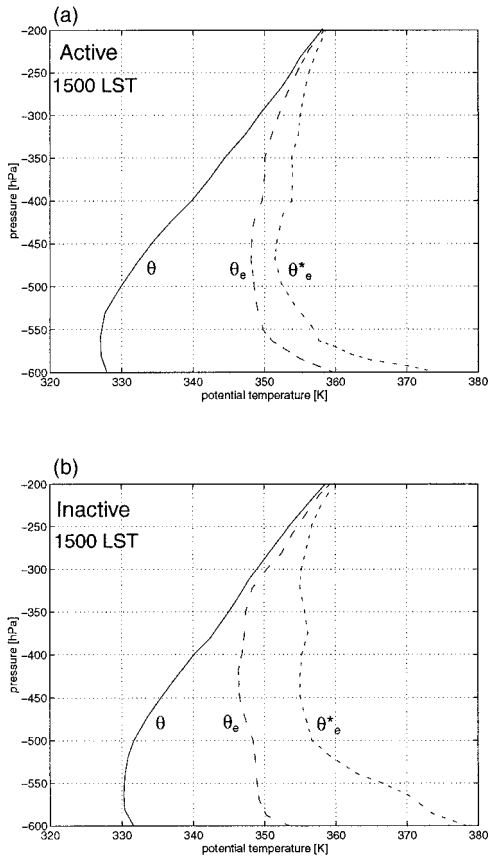


FIG. 10. Mean soundings at 1500 LST for (a) active convection and (b) inactive convection over Visviri. Mean profiles of θ , θ_e , and θ_e^* calculated from rainy and dry composite profiles of air temperature and RH during Visviri I and II.

el Version 5.2 (MM5) to simulate and diagnose the regional processes linking the large-scale and local conditions documented in the previous section. The MM5 is a fully compressible, nonhydrostatic version of a mesoscale numerical model developed by Anthes and Warner (1978). A thorough description of MM5 can be found in Dudhia (1993) and Grell et al. (1994). The MM5 solves the prognostic equations for 3D wind, pressure, temperature, specific humidity, and microphysical variables, using a terrain-following vertical coordinate (σ) and perturbations from a constant reference state of the basic variables (p' , T' , and ρ'). Some of the parameterizations used in this set of simulations are listed in Table 1. Of particular relevance is the inclusion of cloud water, rainwater, and cloud ice in the explicit moisture scheme (Hsie et al. 1984; Dudhia 1989) and the use of the Kain and Fritsch cumulus parameterization scheme (Kain and Fritsch 1993). In the latter scheme, convection is determined by CAPE at the grid point, and once convection is triggered, CAPE is removed in a grid column within an advective time period (Kain and Fritsch 1993). We chose this scheme based on our previous findings of the CAPE–convection relationship

TABLE 1. Physical parameterization used in MM5 for the regional numerical simulations.

Processes	Scheme	References
Cumulus convection	Kain–Fritsch	Kain and Fritsch (1993)
Boundary layer	High-resolution Blackadar	Blackadar (1976)
Moisture	Simple ice	Dudhia (1989)
Radiation	Cloud–radiation	Benjamin and Carlson (1986)
Ground temperature	Force–restore	Blackadar (1976)

over the Altiplano (see Fig. 9) and its good performance in a variety of precipitation scenarios documented in Wang and Seaman (1997).

The model domain consists of a coarse mesh ($\Delta x = \Delta y = 72$ km) that covers most of tropical and subtropical South America, and a nested (one-way interaction), fine mesh ($\Delta x = \Delta y = 24$ km) centered over the central Andes. (The coarse domain is indicated in Fig. 1. The inner domain is shown in Fig. 2.) All the following results, except those relating to the upper-level circulation, are based on the inner domain. Thirty-seven full-sigma levels were used, with the highest resolution in the boundary layer [the lowest half-sigma level ($\sigma = 0.995$) corresponding roughly to 30 m above ground]. Initial and lateral boundary conditions for the model were obtained by interpolating global National Meteorological Center (now known as NCEP) surface and upper-level analysis every 12 h and enhanced by synoptic observations assimilated using the Cressman scheme. Given the current computational limitations, we decided to integrate the model for 60 h during a pair of rainy and dry episodes selected on the basis of the index of convection (CI^*), where highly contrasting signatures of convective cloudiness over the Altiplano are readily evident in the B3 ISCCP infrared images³ shown in Fig. 11. The rainy simulation begins at 2100 LST 15 January 1993, and the dry simulation begins at 2100 LST 5 February 1993. In both cases, the first 9 h or so are taken as the model’s spinup period, yielding simulations of two full diurnal cycles. Within each simulation, the diurnal marches of the atmospheric conditions are similar, and we merged some of the model outputs at the same time of day 1 and 2 into rainy or dry *event* means. For instance, fields at 1100 LST of the rainy event are the simple average of the 1100 LST output of day 1 (16 January) and day 2 (17 January) of the rainy simulation.

³ Despite local observations in Visviri during parts of January of 1994 and 1995, we chose to simulate two episodes during the summer of 1993 given the availability of ISCCP B3 images and the more complete set of synoptic observations during the summer of 1993 used in the model initialization.

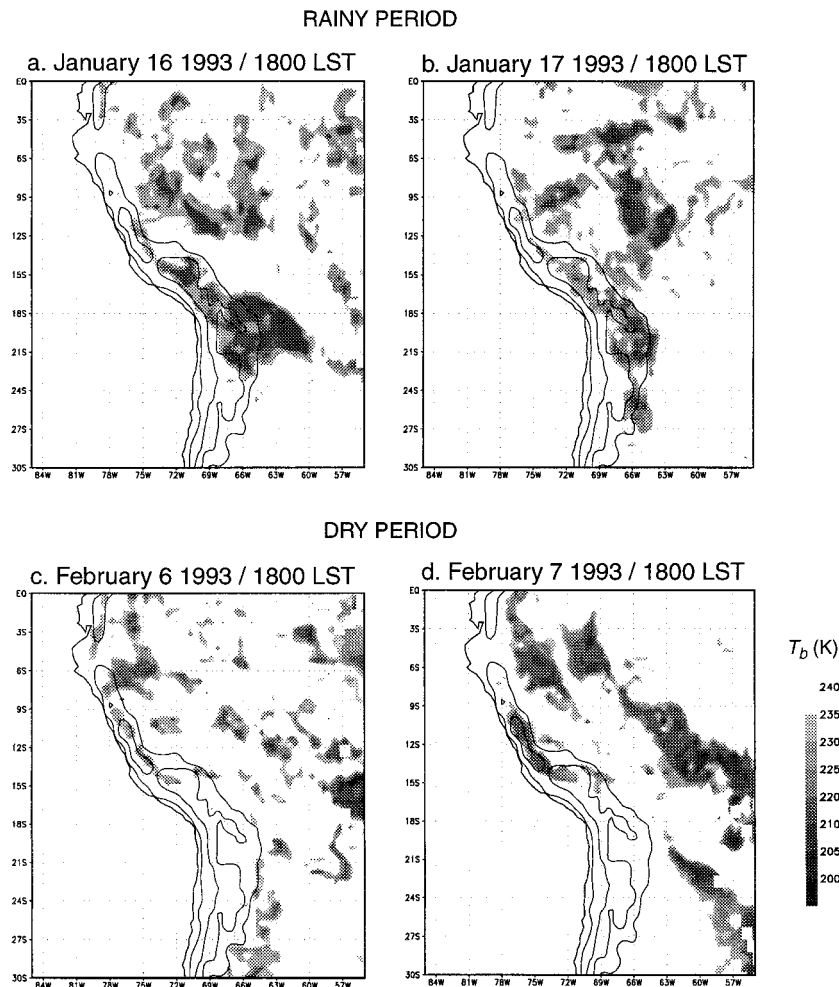


FIG. 11. *GOES-7* infrared temperature at 1800 LST for (a) 16 Jan 1993, (b) 17 Jan 1993, (c) 6 Feb 1993, and (d) 7 Feb 1993. The 2000- and 4000-m topographic contours are indicated by solid lines.

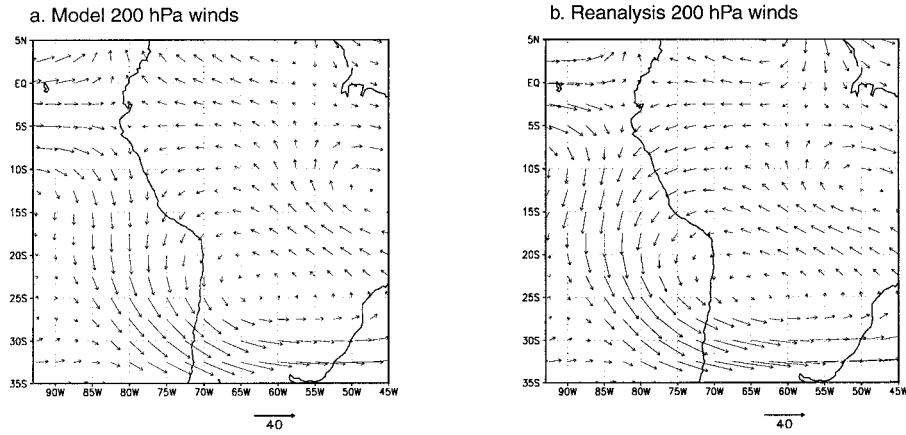
b. Model results

Figure 12 shows the model winds at 200 hPa, 36 h after initialization, for both rainy and dry simulations, together with the corresponding NCEP–NCAR reanalyses. The evolution of the upper-level conditions during the 60-h simulation is rather slow, and hence the patterns in Fig. 12 are representative of the whole period. Comparison between model output and observations (reanalyses) reveals that the model realistically simulates the large-scale upper-level flow in both cases. Consistent with our previous discussion, the upper-level flow during the rainy event is characterized by a well-defined anticyclone centered at 25°S, 65°W. At 500 hPa (not shown) the anticyclone is still evident, although its center has shifted westward over the subtropical Andes, and easterly flow of about 5 m s⁻¹ crosses the central Andes between 14° and 21°S. In contrast, during the dry period the subtropical circulation is dominated by a midlatitude trough, whose axis coincides with the An-

dean ridge south of 20°S, and a strong subtropical jet crossing the central Andes, with westerly winds in excess of 10 m s⁻¹ at the 500-hPa level.

A qualitative, yet particularly relevant, measure of the overall model performance is given in Fig. 13, which shows the simulated cloud-top temperature at 1800 LST for rainy and dry simulations. Comparison with brightness temperature images from *GOES-7* (Fig. 11) reveals good agreement between the observed and simulated cold cloud coverage, with most of the central Andes covered with convective cloudiness during the afternoons of the rainy period and cloud free during the dry period. The model tends to predict too many cold clouds around sunrise, but the simulated contrast between rainy and dry conditions is similar to the observed (not shown). Besides the general correspondence, the model seems to realistically simulate the location, shape, and intensity of cloud clusters over the southern Altiplano, the eastern slope of the Andes, and

January 17 1993. 1200 UTC (36-h wet)



February 7 1993. 1200 UTC (36-h dry)

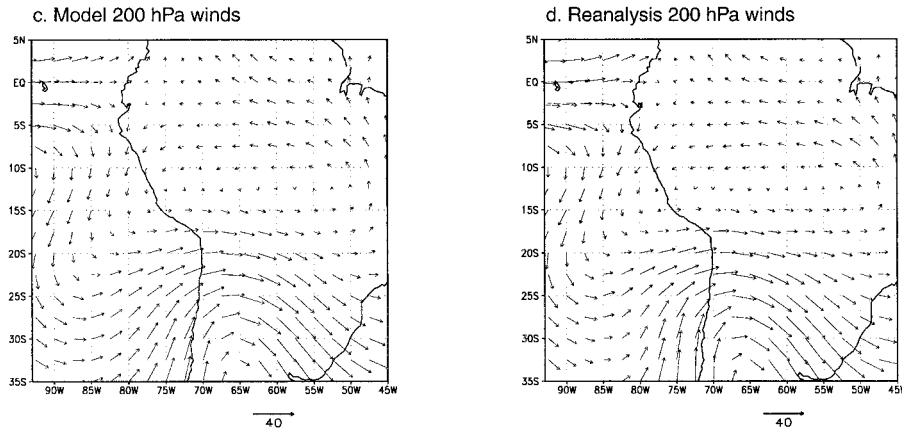


FIG. 12. (a) Model (outer domain) 200-hPa winds at 1200 UTC 17 Jan 1993 (36 h after initialization of the rainy simulation) interpolated to $2.5^\circ \text{ lat} \times 2.5^\circ \text{ long}$ grid. (b) NCEP–NCAR reanalysis 200-hPa winds at 1200 UTC 17 Jan 1993. (c) As in (a) but for 1200 UTC 7 Feb 1993 (36 h after initialization of the dry simulation). (d) As in (b) but for 1200 UTC 7 Feb 1993.

the eastern lowlands. In the rainy case, roughly 70% of the model daytime (0600–2100 LST) rainfall is convective (nonexplicit) with a spatial average of about 7 mm per 12 h (local maxima in excess of 12 mm per 12 h) over the Altiplano.

The topography and horizontal wind field at the lowest half-sigma level (hereafter referred to as surface winds) for the afternoon (1500–1700 LST) of the rainy and dry simulations are displayed in Fig. 14. In the dry case, a northwesterly low-level jet is found over the lowlands to the east of the central Andes between 10° and 20°S , with surface winds in excess of 10 m s^{-1} . The jet, forced by a deepened thermal low over northwestern Argentina ($\sim 25^\circ\text{S}$), tends to decelerate the daytime upslope flow over the lower part of the eastern side of the Andes due to the Coriolis force. In the rainy composite, the surface flow east of the Andes is much weaker and distorted, and the model consistently sim-

ulates a stronger terrain-normal daytime flow over the eastern foothills, particularly around 16°S . Over most of the Altiplano, surface winds are in the same direction as the flow aloft (easterly in the rainy case, westerly in the dry case), producing an elongated region of strong low-level convergence with the upslope flow from the opposite direction. The simulated patterns of the low-level wind are evident to some degree in the sparse surface observations over and around the central Andes included in Fig. 14.

Further details of the diurnally varying regional flow are displayed in section AA' extending across the central Andes (Fig. 15), which shows the wind normal to the barrier at 0300, 1100, and 1600 LST for the rainy and dry events, and from the traces of wind speed at points H (3500 m, near the Altiplano) and L (700 m, near the foothill) over the eastern slope of the Andes (Fig. 16). The results in Fig. 15 are fairly representative of other

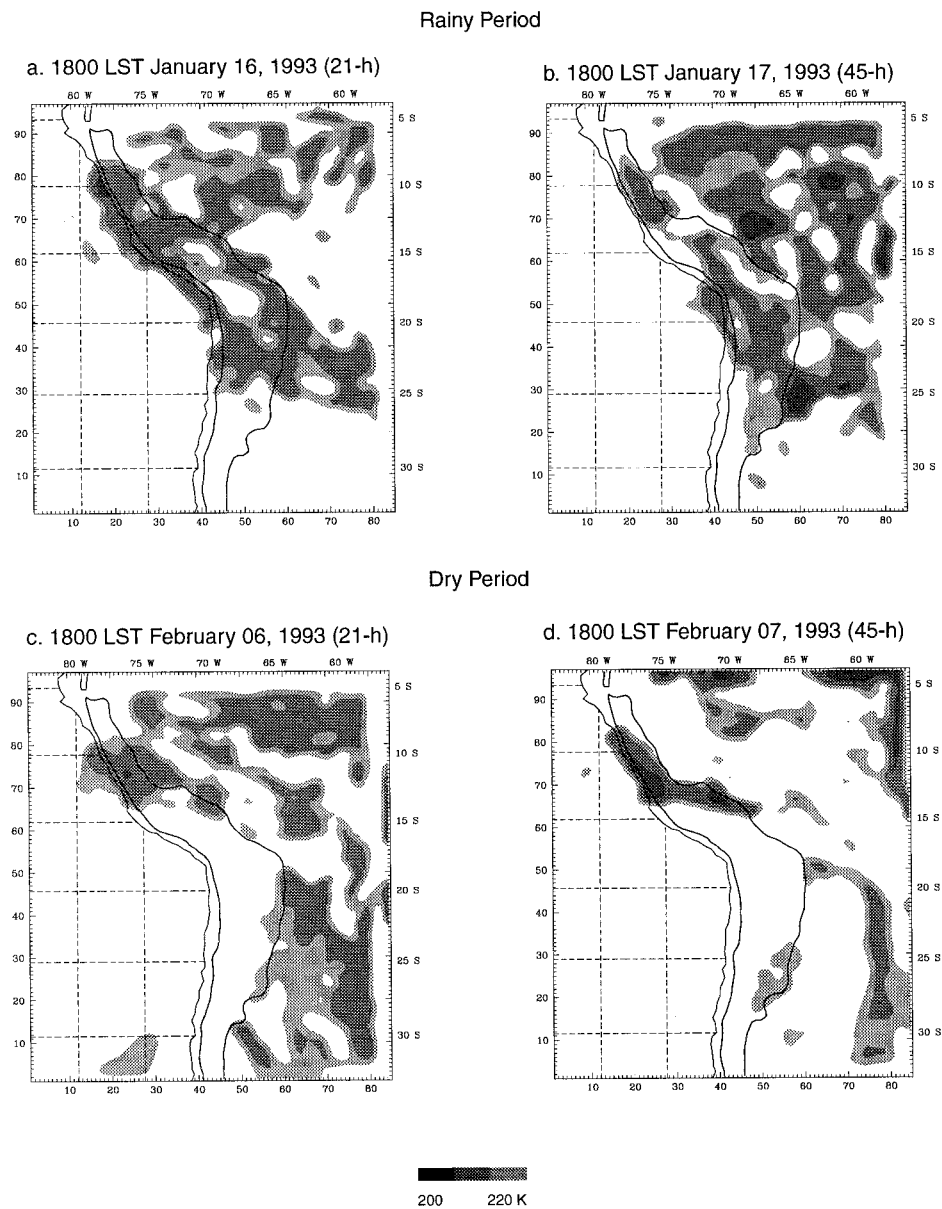


FIG. 13. Simulated cloud-top temperature (CTT) at 1800 LST for rainy and dry simulations. Light and dark shading indicate CTT below 220 and 205 K, respectively. (a) 16 Jan 1993 (21 h after initialization of the rainy simulation). (b) 17 Jan 1993 (45 h after initialization of the rainy simulation). (c) 6 Feb 1993 (21 h after initialization of the dry simulation). (d) 7 Feb 1993 (45 h after initialization of the dry simulation). In all panels, the 2000-m topographic contour is indicated by a solid line.

sections taken across the central Andes (not shown). The nocturnal regime, characterized by downslope flow and statically stable stratification, begins around sunset in both simulations. In the dry simulation, the downslope flow over the eastern slope runs well into late morning, reaching a maximum speed in excess of 5 m s^{-1} around 0300 LST (Fig. 15b). In the rainy case, the westerly downslope flow is weaker and shallower (Fig. 15a), particularly along the upper half of the slope where it is capped by easterly winds aloft, and it ends within an hour of the sunrise (Fig. 16a). As the surface warms

up throughout the day, a convective boundary layer (CBL) develops over the sloping terrain and the Altiplano (Fig. 17) and daytime upslope flow sets in. Over the steeper western side, the upslope flow is shallow and strong ($h \sim 600\text{ m}$, $u \sim 8\text{ m s}^{-1}$) in both the rainy and dry simulations. Near the eastern foothills (point L), the daytime flow in the rainy simulation is just slightly stronger than its dry counterpart, with maximum speeds of about 4 m s^{-1} during the midafternoon (Fig. 16). However, the strength and extent of the upslope flow over the middle and upper part of the eastern side

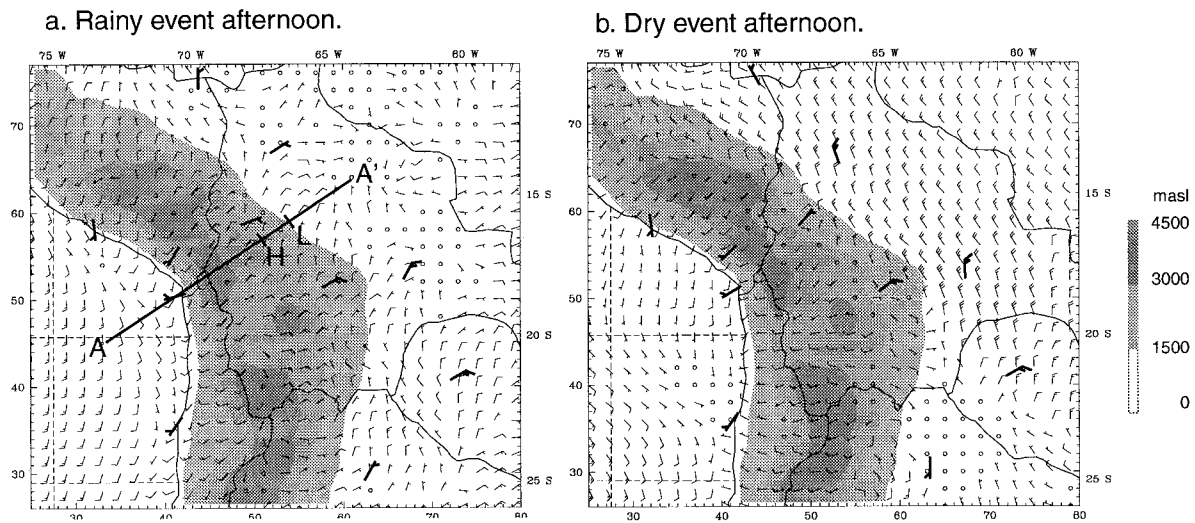


FIG. 14. (a) Surface winds ($\sigma = 0.995$, ~ 30 m AGL) during afternoon of the rainy event. The event mean was calculated as the average of the half-hourly model output between 1500 and 1700 LST of days 1 and 2 of the rainy simulation. Full barb: 10 kt. Shading represents terrain elevation. Cross section AA' referred to in subsequent figures. Thick barb vectors are synoptic surface observations. (b) As in (a) but for the afternoon of the dry event.

of the Andes is significantly larger in the rainy case. During the two rainy afternoons, upslope flow appears over point H before 1200 and accelerates until 1700 LST to attain speeds in excess of 6 m s^{-1} (Fig. 16a), nearly twice the maximum upslope flow speed during the dry afternoons (Fig. 16b).

Examination of the hourly output during the rainy simulation reveals that the strong easterly upslope flow within the CBL ($h \sim 1600$ m, $u \sim 6 \text{ m s}^{-1}$) reaches the Altiplano by 1200 LST (Fig. 15c), followed by a westward incursion of potentially colder air. Intense low-level convergence between this flow and surface westerly winds, originating in the western side of the Andes, is found over the central part of the plateau during afternoon and early evening (Fig. 15e, see also Fig. 14a) and the resulting region of upward motion extends from the surface to 230 hPa. In contrast, the weaker easterly upslope flow (capped by westerly winds aloft) never reaches the Altiplano in the dry event, and its convergence with the lower branch of a mountain-wave circulation takes place over the eastern slope of the Andes (Fig. 15f, see also Fig. 14b) in the so-called leeside convergence zone (Banta 1986). In this latter case, the mesoscale upward motion grows up to only 450 hPa, limited by upper-level subsidence within the mountain wave aloft.

Consistent with the differences in the strength and extent of the upslope flow over the eastern side of the Andes, the water vapor distribution exhibits a marked contrast between the rainy and dry simulations (Fig. 18). Notice that over the foothills and lowlands to the east of the central Andes, the mixing ratio in the lower and middle troposphere is slightly higher ($\sim 1.0 \text{ g kg}^{-1}$) during the dry event. Early in the morning, the mixing ratio

profile along the eastern slope is fairly similar in the two events, decreasing upward to values less than 4 g kg^{-1} over the Altiplano (Figs. 18a,b). During the late morning and early afternoon of the rainy simulation, the surface easterly flow transports significant amounts of water vapor within the CBL, increasing the mixing ratio over the Altiplano up to 8 g kg^{-1} , and a tall plume of cloud and rainwater develops over the plateau (Fig. 18e) collocated with the mesoscale region of upward motion. In contrast, in the dry event the moisture transport from the lowlands to the east of the Andes is restricted to the upper half of the eastern slope, and the maximum afternoon low-level mixing ratio over the Altiplano does not exceed 5 g kg^{-1} (Fig. 18f). The effect of the middle-level flow is also evident in Fig. 18: easterly winds advect water vapor within the CBL, producing a plume of moist air to the west of the Andes in the rainy simulation, whereas entrainment of dry air from the west tends to dry out the otherwise moist CBL over the upper half of the eastern slope of the Andes.

Over the very dry western slope of the Andes, the model simulates values of a water vapor mixing ratio of similar magnitude to the values simulated over the much humid eastern slope, which is suggestive of an excessive upslope moisture transport from the coastal areas of northern Chile and southern Peru. This problem might arise from the absence of a coastal escarpment in the model topography, which in reality laterally confines the moist air within the marine boundary layer over the eastern Pacific. Nevertheless, only air parcels originating in the eastern foothills can become positively buoyant. A closer examination of this point is based on Fig. 19a, which shows the equivalent potential temperature and air parcel trajectories along the AA' transect

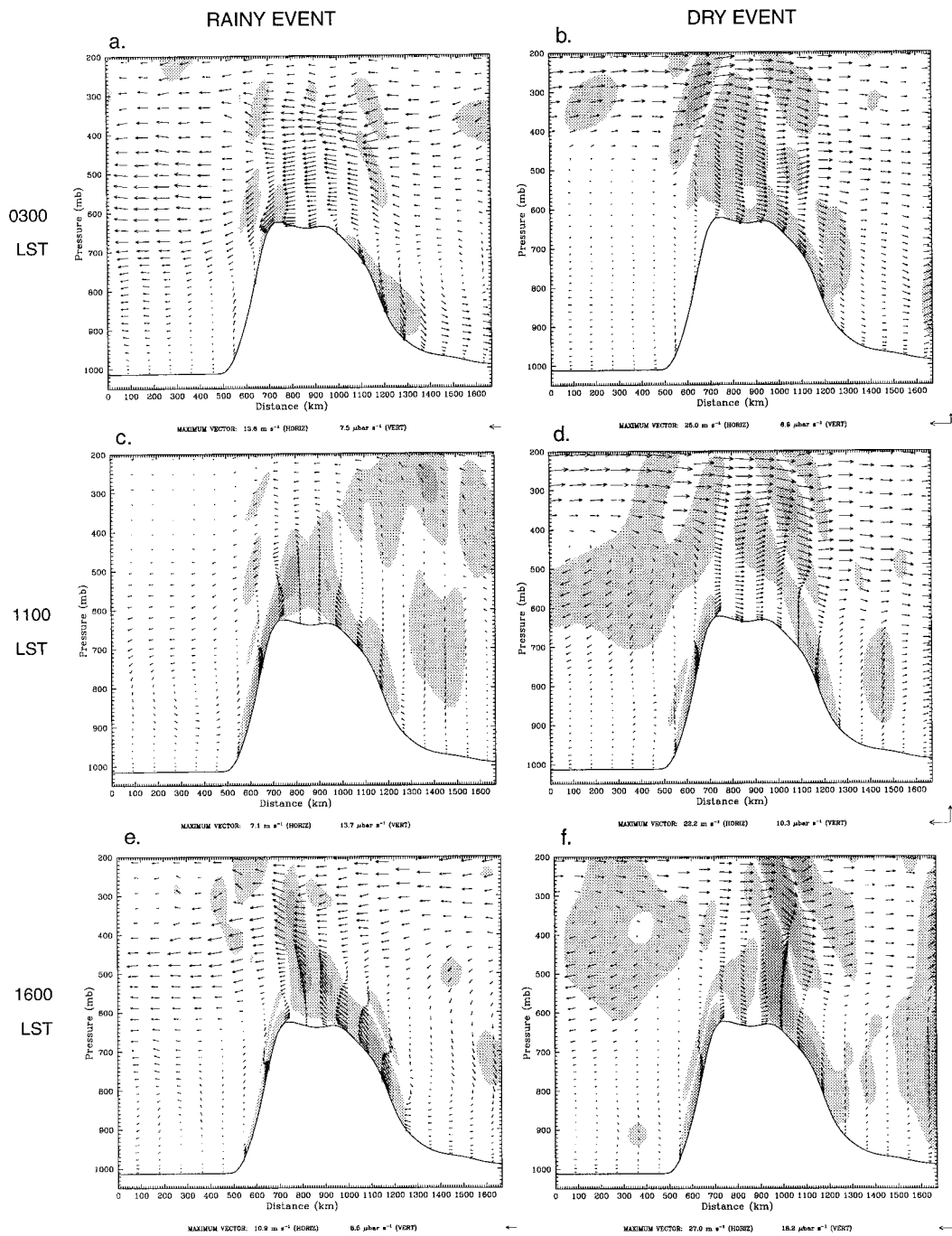


FIG. 15. Wind vectors normal to the Andes cross section AA' (Fig. 14). Shading indicates vertical velocities larger than +2.5 cm s⁻¹ or less than -2.5 cm s⁻¹. (a) 0300 LST rainy event (average of 0300 LST of days 1 and 2 during the rainy simulation). (c) 1100 LST rainy event. (d) 1600 LST rainy event. (b) As in (a) but for the dry event. (d) As in (c) but for the dry event. (f) As in (e) but for the dry event.

at 1600 LST of the rainy event. The trajectories begin at 1030 LST and were calculated using 30-min output of the 3D wind field interpolated down to 5 min. Since the wind component normal to the cross section is weak ($v < 1 \text{ m s}^{-1}$) the trajectories are essentially contained

within this plane. High θ_e ($\sim 343 \text{ K}$) air parcels originating in the boundary layer on the lowlands to the east of the Andes are channeled toward the eastern slope, reaching the Altiplano about 6 h later, and, assuming they remain undiluted, most of them become positively

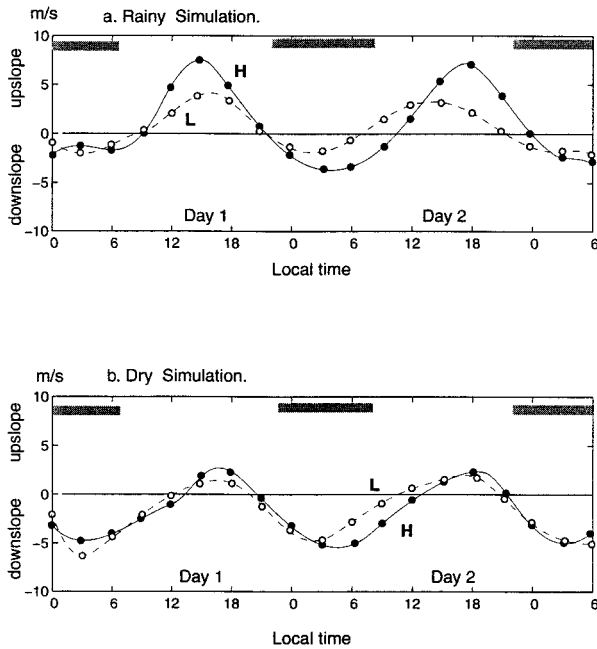


FIG. 16. (a) Wind speed along the eastern slope of the Andes at points L (near the foothill, dashed line) and H (near the Altiplano, solid line), indicated in Figs. 14 and 15, for days 1 and 2 of the rainy simulation. Gray bars at the top indicate nighttime. (b) As in (a) but for days 1 and 2 of the dry simulation. The 30-min output was filtered using a 7-point running mean filter in time.

buoyant [$\theta_e(\text{parcel}) > \theta_e^*(\text{environment})$] within the mesoscale region of upward motion over the plateau. In contrast, the highest θ_e over the western foothills (~ 333 K) is well below that of the minimum midtropospheric $\theta_e^* \sim 340$ K, and therefore, even though the simulated daytime flow over the western slope of the Andes may increase the water vapor content over the Altiplano, it does not contribute to the buildup of potential instability required for the subsequent development of cumulus convection. In the dry case, the air over the Altiplano has low θ_e (~ 325 K; Fig. 19b), which is consistent with its origin in the western foothills and slopes, and, consequently, it cannot support convective activity, even in the presence of localized updrafts over the Altiplano.

c. Model diagnosis

The wind direction in the middle troposphere over the Altiplano seems to be a key element in controlling the strength of the daytime flow over the eastern slope of the Andes, especially in the upper portion of the sloping terrain where the top of the CBL reaches the 500-hPa level. A tendency for surface winds over sloping terrain to be in the same direction of the winds aloft, and, more generally, the influence of the large-scale, ridge-top winds on the intensity and extent of the regional upslope flow, has also been documented in observational studies (Banta 1984; Wolyn and McKee 1994) and in numerical simulations (Banta 1986; Bos-

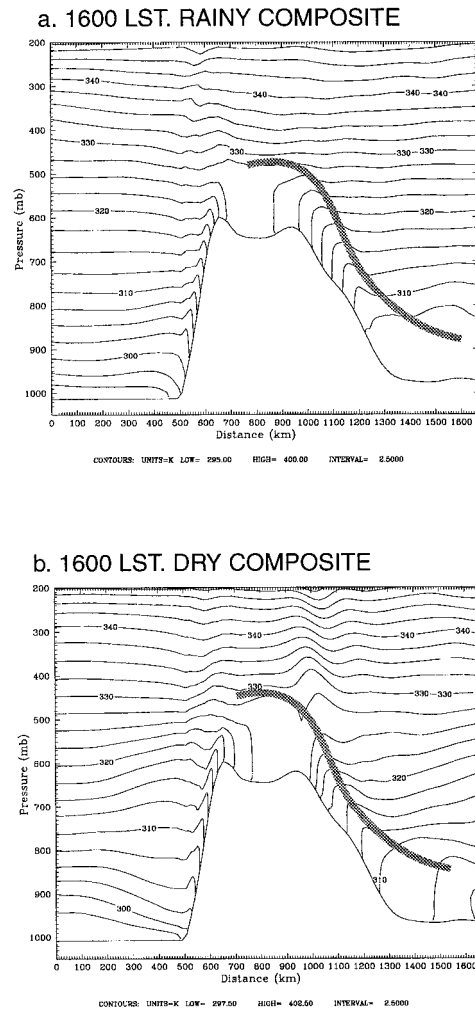


FIG. 17. Potential temperature (contour every 2.5 K) across section AA' (Fig. 17). (a) 1600 LST rainy event (average of 0300 LST of days 1 and 2 of the rainy simulation). (b) 1600 LST dry event. Thick line indicates the top of the CBL.

sert and Cotton 1994) over the eastern slope of the Rockies.

To quantify this effect, we made a diagnosis of the momentum balance of the winds within the CBL over point H (Fig. 15a) using the model output at noontime for day 2 in the rainy and dry simulations. From a regional perspective, the eastern slope of the Andes is rather gentle ($\tan\alpha \sim 3.3$ km per 250 km) and uniform. Assuming a 2D geometry in the plane where the slope is contained (i.e., the cross section AA' in Fig. 15 repeats infinitely in the axis normal to AA'), integration of the along-slope momentum equation over the depth of the CBL (H) yields (e.g., Barry 1992):

$$\bar{u}_t + \bar{u}\bar{u}_x = g\frac{\Delta\theta}{\theta_0} \sin\alpha + \cos\alpha\frac{g}{\theta_0} [(\Delta\theta)H]_x + f\bar{v} + FR, \tag{1}$$

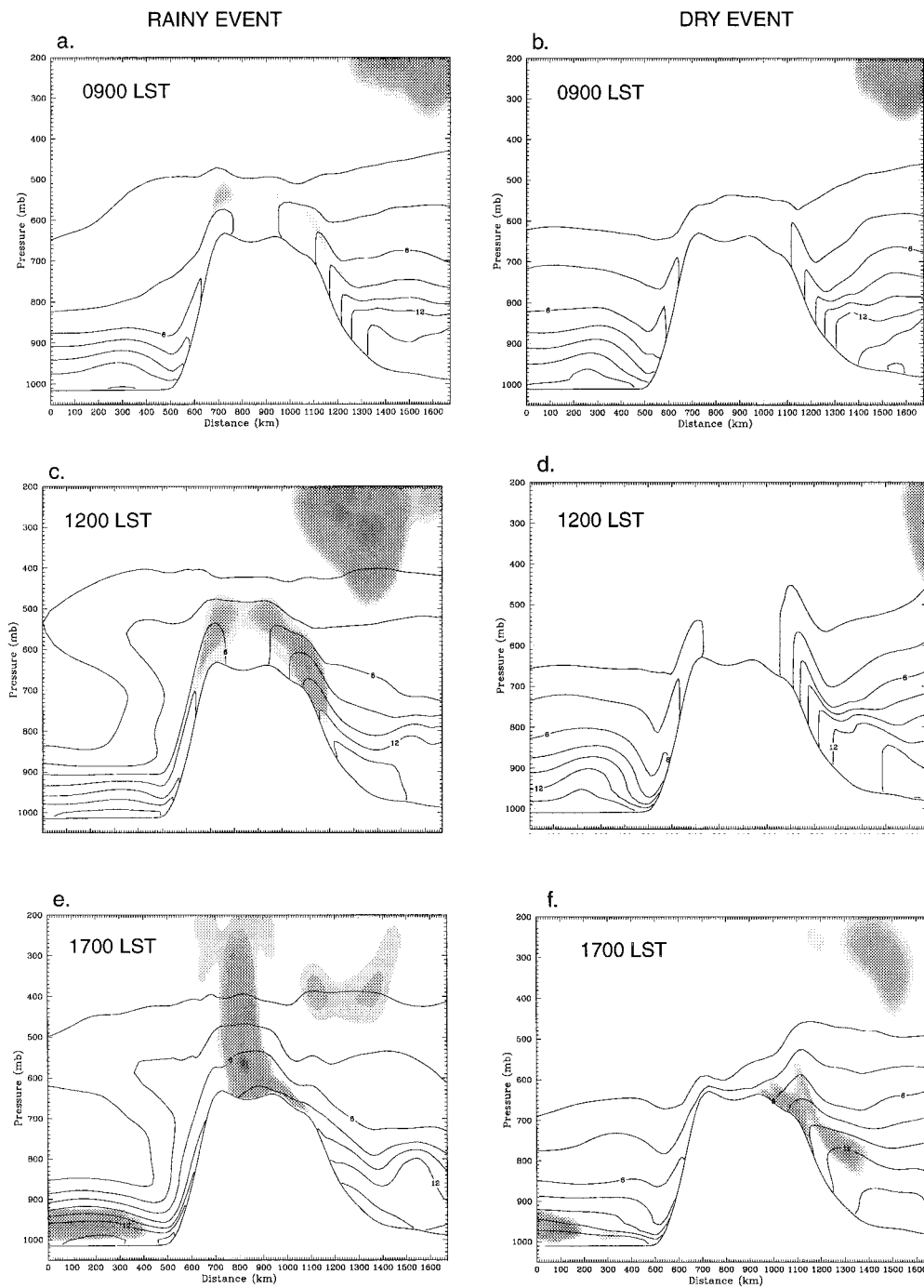


FIG. 18. Mixing ratio (contour each 2 g kg^{-1}) across section AA' (Fig. 17). Light, medium, and dark shading indicate cloud plus rainwater in excess of 0.25, 0.75, and 1.0 g kg^{-1} , respectively. (a) 0900 LST rainy event (average of 0900 LST of days 1 and 2 of the rainy simulation). (c) 1200 LST rainy event. (d) 1700 LST rainy event. (b) As in (a) but for the dry event. (d) As in (c) but for the dry event. (f) As in (e) but for the dry event.

where the subscripts refer to partial derivatives, x is the along-slope coordinate, \bar{u} is the mean (vertically averaged) along-slope wind component (upslope flow), \bar{v} is the mean wind component normal to the plane of the slope, $\Delta\theta$ is the potential temperature excess of the air

near the sloping terrain with respect to the air outside the CBL, and θ_0 is a basic-state reference potential temperature outside the CBL. The forcing terms on the rhs of Eq. (1) are the buoyancy force, the thermal wind, the Coriolis force, and friction, respectively. The frictional

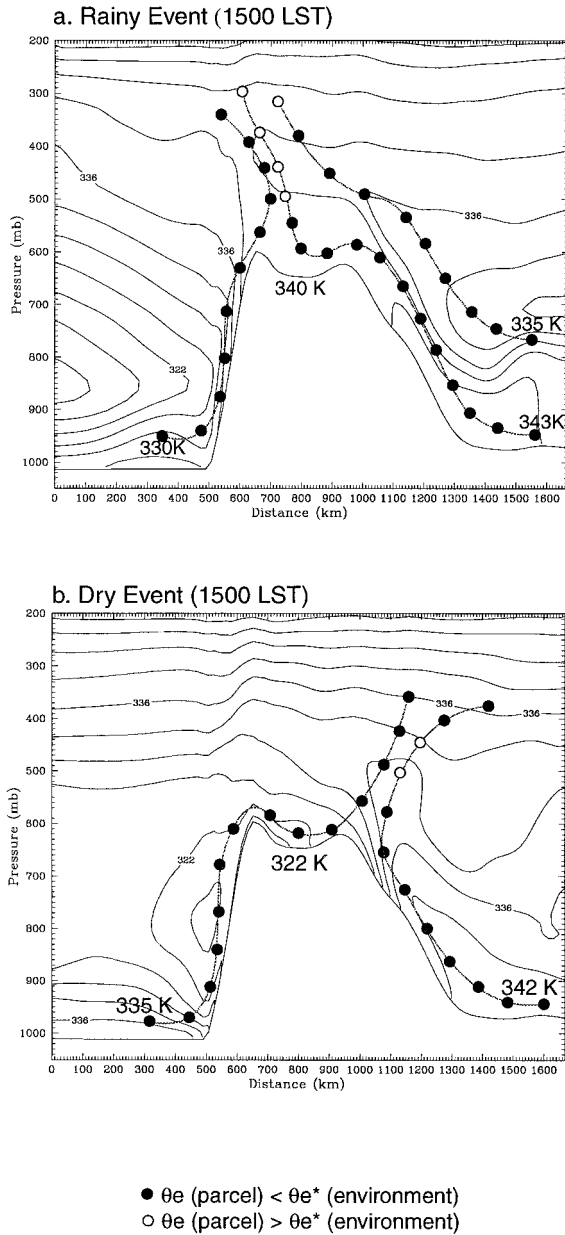


FIG. 19. Equivalent potential temperature (θ_e , contour every 3.5 K) at 1600 LST and air parcel trajectories across section AA' (Fig. 17). See text for details of the trajectories calculation. Air parcels are released at 1030 LST, and their subsequent positions are plotted each 30 min by a filled circle (if the original θ_e of the air parcel is less than the ambient θ_e^*) or open circle (otherwise). (a) Rainy event. (b) Dry event.

term was parameterized as the divergence throughout the CBL of the surface friction and the vertical entrainment from aloft:

$$FR = (w_e \Delta u_i - C_D u^2)/H, \quad (2)$$

where w_e is the entrainment velocity, Δu_i is the wind shear across the top of the CBL, and C_D is the surface drag coefficient. Both w_e and C_D were estimated as a

TABLE 2. Along-slope momentum balance over point H (see Fig. 17) at 1200 LST of day 2. See text for details. Plus and minus signs indicate upslope and downslope acceleration.

Term	Magnitude ($10^4 \times \text{m s}^{-2}$)	
	Wet case	Dry case
Along-slope advection	-0.4	-0.5
Buoyancy	+2.2	+2.3
Thermal wind	+1.3	+1.3
Coriolis force	+0.1	+0.1
Surface friction	-0.3	-0.2
Vertical entrainment	+0.8	-0.9
Observed rate of change	+3.7	+2.1
Calculated rate of change	+3.3	+1.7

function of the surface heat flux and local static stability using the expressions given in Stull (1989, section 7).

The magnitude of each term in Eq. (1) is given in Table 2. As expected, the main driving forces for the daytime upslope flow are the thermal contrast between the heated sloping terrain and the colder air in the free atmosphere (the buoyancy term) and the increase of potential temperature along the slope (the thermal wind term). The similar magnitude of these two terms in the rainy and dry cases is consistent with the similar daytime thermal structure that develops over the Andes in both simulations (Fig. 17). The along-slope advection and the Coriolis force are an order of magnitude smaller and also comparable in the two cases. The deceleration due to surface friction is slightly stronger in the rainy case, but the main difference in the momentum balance is largely produced by the vertical entrainment term, which is of opposite sign in the rainy and dry simulations. In the rainy case, turbulent mixing across the top of the inversion entrains air with easterly momentum, accelerating the upslope flow over the eastern slope of the Andes. In contrast, westerly winds over the CBL during the dry simulation tend to decelerate the easterly upslope flow within the CBL by entraining air with momentum of opposite sign (westerly). The net result is that the local rate of change of the along-slope wind in the dry case is about half of that calculated in the rainy case, which is consistent with the subsequent weak (strong) easterly upslope flow observed in the dry (rainy) simulation.

6. Conclusions

Low-level conditional instability over the South American Altiplano prevails on most summertime afternoons, a consequence of the intense solar heating of the surface and the moisture contrast between air within the local boundary layer and the air aloft (~ 500 hPa). Nevertheless, this instability can be released only on days in which the near-surface specific humidity (q_{LL}) reaches high values ($\sim 7 \text{ g kg}^{-1}$ or more), yielding saturation of near-surface air parcels by the time they reach about 50 hPa above the ground. These days tend to

cluster in “rainy” episodes that last between 4 and 10 days and account for most of the summertime rainfall over the central Andes. Alternating dry episodes are characterized by low values of mixing ratio within the CBL ($\sim 4 \text{ g kg}^{-1}$ or less) and an absence of convective cloudiness. These thresholds of q_{LL} must be regarded as simple references, as they are deduced from rainfall and mixing ratio observations at a single station over the Altiplano (Visviri) taken during two summers (section 4b). Yet the variability of the near-surface mixing ratio ($\sim 3 \text{ g kg}^{-1}$) between rainy and dry episodes inferred from the local observation is in close agreement with the difference of reanalyzed mixing ratio at 600 hPa between composite rainy and dry episodes based on a 17-summer record (cf. Figs. 5d and 6d).

Our compositing analysis has shown that rainy and dry episodes over the central Andes are associated with well-defined continental-scale anomalies in convection and upper- and middle-level circulation, confirming and extending previous results based on more limited datasets (e.g., Aceituno and Montecinos 1993; Lenters and Cook 1999; Vuille et al. 1998). Rainy episodes over the Altiplano occur simultaneously with well-defined anticyclonic, equivalent barotropic anomalies over subtropical South America (centered at 25°S), leading to easterly winds over the central Andes. The opposite situation (cold core cyclone) prevails during dry episodes, with the central Andes exposed to westerly winds. These circulation anomalies substantially reinforce or weaken the climatological Bolivian High and seem primarily forced by low frequency, planetary waves originating in the Southern Hemisphere extratropics. The large-scale “signal” in the lower troposphere is much weaker and less distinctive. In particular, the reanalyzed low-level mixing ratio anomalies to the east of the Andes (the source region of high θ_e air) are not substantially different in the rainy and dry composites and are too small ($\sim 1 \text{ g kg}^{-1}$) to explain the moisture variability over the Altiplano ($\sim 3 \text{ g kg}^{-1}$) between rainy and dry episodes. The reason for this could be the poor resolution of the reanalysis data in comparison with the Andean geography, or, alternatively, the existence of several low-level patterns associated with rainfall departures over the Altiplano, as recently suggested by Lenters and Cook (1999) and Vuille et al. (1998).

To gain insight into the regional processes linking the large and local conditions, we have used a numerical mesoscale model with a horizontal resolution of 24 km. Comparison of the model output with synoptic observations, reanalysis fields, and satellite images of convective cloudiness indicates that the model realistically simulates two contrasting rainy and dry episodes. The most marked and relevant differences between simulations are the intensity, timing, and extent of the diurnally varying upslope flow over the eastern slope of the Andes. During the rainy simulation, strong easterly winds within the CBL reach the upper part of the eastern slope of the Andes by midmorning, followed by a west-

ward intrusion of high θ_e air (originating in the eastern lowlands) into the Altiplano during the early afternoon. In this case, surface easterly winds prevail over the Altiplano, in the same direction as the flow aloft, and low-level convergence is found over the plateau collocated with the axis of maximum daytime precipitation. In contrast, during dry periods the moisture transport from the east is restricted somewhere over the eastern slope of the Andes, the surface of the Altiplano is dominated by westerly winds, and the plateau is flooded by low θ_e air originating in the western foothills and slopes. Despite the existence of a well-defined leeside convergence zone, deep convection is suppressed over the eastern side of the Andes by the midlevel entrainment of dry air and subsidence forced by mountain-wave circulation.

A diagnosis of the momentum balance within the CBL over the upper half of the eastern slope of the Andes indicates that the contrast in the daytime upslope flow between rainy and dry simulations are largely produced by differences in the vertical entrainment of momentum at the top of the CBL. In both cases, the upslope flow is mainly driven by the upper-level heat source that develops over the mountainous terrain. In the rainy case, the westward large-scale flow at the ridge level produces turbulent entrainment of easterly momentum across the top of the inversion that tends to accelerate the easterly upslope flow. In contrast, midtropospheric eastward winds during the dry simulation tend to decelerate the easterly upslope flow within the CBL, by entraining air with momentum of opposite sign.

It must be stressed that our conclusions regarding the local- and regional-scale processes over the central Andes are based on a short, single-site observational record and a pair of short-term numerical simulations, and therefore they might lack generality. Yet the model results suggest a plausible, physically consistent linkage between the slowly varying large-scale anomalies in the upper- and middle-level circulation and the local thermodynamic conditions over the Altiplano that support or suppress deep convection through the diurnally varying, regional-scale flow over the eastern slopes of the Andes. A more conclusive picture of the rainy and dry conditions over the central Andes will have to wait until in situ enhanced observations over the Altiplano and the slopes of the Andes yield a more thorough validation of numerical and conceptual models.

Acknowledgments. The author gratefully acknowledges many helpful comments and advice provided by Drs. John M. Wallace and Patricio Aceituno. Thanks are also due to Dr. John Lenters for a very thorough and helpful review of the manuscript and to the other reviewer who helped improve this work. Drs. Brian Colle, Kerry Cook, and Brad Smull also offered many useful comments. Ken Westrick kindly helped in handling the mesoscale model. NCEP–NCAR reanalysis data was provided through the NOAA Climate Diagnostics Center. The B3 ISCCP data were obtained from NASA/

Langley Research Center EOSDIS Distributed Active Archive Center. The field experiments Visviri I and II were part of a research project of the Department of Geophysics of the University of Chile, supported by Grants Fondecyt (Chile) 1930789 and IPGH Geof 93.26. Dr. Patricio Aceituno and Aldo Montecinos kindly provided the data from Visviri I and II. The author is partially supported by the National Science Foundation under Grant 9215512 and by the Department of Geophysics of the University of Chile.

REFERENCES

- Aceituno, P., 1997: Climate elements of the South American Altiplano. *Rev. Geofis.*, **44**, 37–55.
- , and A. Montecinos, 1993: Circulation anomalies associated with dry and wet periods in the South American Altiplano. *Proc. Fourth Int. Conf. on Southern Hemisphere Meteorology*, Hobart, Australia, Amer. Meteor. Soc., 330–331.
- , and R. Garreaud, 1995: The impact of the ENSO phenomenon in the pluviometric regime over the Andes. *Rev. Chil. Ing. Hidraul.*, **2**, 33–43.
- , and A. Montecinos, 1997a: Patterns of convective cloudiness in South America during austral summer from OLR pentads. Preprints, *Fifth Int. Conf. on Southern Hemisphere Meteorology and Oceanography*, Pretoria, South Africa, Amer. Meteor. Soc., 328–329.
- , and —, 1997b: Meteorological field experiments in the South American Altiplano. Preprints, *Fifth Int. Conf. on Southern Hemisphere Meteorology and Oceanography*, Pretoria, South Africa, Amer. Meteor. Soc., 330–331.
- , H. Fuenzalida, and J. Rutllant, 1995: Meteorological field experiment “Visviri I” in the South American Altiplano. *Proc. 19th Annual Climate Diagnostics Workshop*, College Park, MD, Amer. Meteor. Soc., 19–21.
- Anthes, R. A., and T. T. Warner, 1978: Development of hydrodynamic models suitable for air pollution and other mesometeorological studies. *Mon. Wea. Rev.*, **106**, 270–286.
- Banta, R. M., 1984: Daytime boundary-layer evolution over mountainous terrain. Part I: Observations of the dry circulations. *Mon. Wea. Rev.*, **112**, 340–356.
- , 1986: Daytime boundary-layer evolution over mountainous terrain. Part II: Numerical studies of upslope flow duration. *Mon. Wea. Rev.*, **114**, 1112–1130.
- , 1991: The role of the mountain flow making clouds. *Atmospheric Processes over Complex Terrain*, Meteor. Monogr., No. 23, Amer. Meteor. Soc., 183–203.
- Barry, R. G., 1992: *Mountain Weather and Climate*. 2d ed. Rutledge, 402 pp.
- Benjamin, S. G., and T. N. Carlson, 1986: Some effects of surface heating and topography on the regional severe storm environment. Part I: Three-dimensional simulations. *Mon. Wea. Rev.*, **114**, 975–1001.
- Blackadar, A. K., 1979: High resolution models of the planetary boundary layer. *Advances in Environmental Sciences and Engineering*, J. Pfafflin and E. Ziegler, Eds., Vol. 1, Gordon and Breach Scientific, 50–85.
- Bossert, J. E., and W. R. Cotton, 1994: Regional-scale flows in mountainous terrain. Part II: Simplified numerical experiments. *Mon. Wea. Rev.*, **122**, 1472–1489.
- Dempsey, D., 1996: Spatial-differencing errors in MM5’s terrain-following coordinate. *Proc. Sixth PSU/NCAR Mesoscale Model User’s Workshop*, Boulder, CO, NCAR, 82–85.
- Dudhia, J., 1989: Numerical study of convection observed during the winter monsoon experiment using a mesoscale two-dimensional model. *J. Atmos. Sci.*, **46**, 3077–3107.
- , 1993: A nonhydrostatic version of the Penn State/NCAR mesoscale model: Validation test and simulation of an Atlantic cyclone and cold front. *Mon. Wea. Rev.*, **121**, 1493–1513.
- Figueroa, S. N., P. Satyamurty, and P. L. Silva Dias, 1995: Simulation of the summer circulation over the South American region with an Eta coordinate model. *J. Atmos. Sci.*, **52**, 1573–1584.
- Fuenzalida, H., and J. Rutllant, 1987: Origen del vapor de agua que precipita sobre el Altiplano de Chile. *Proc. II Congreso Interamericano de Meteorología*, Buenos Aires, Argentina, 6.3.1–6.3.4.
- Garreaud, R. D., and J. M. Wallace, 1997: The diurnal march of convective cloudiness over the Americas. *Mon. Wea. Rev.*, **125**, 3157–3171.
- Grell, G. A., J. Dudhia, and D. R. Stauffer, 1994: A description of the fifth-generation Penn State/NCAR mesoscale model. NCAR Tech. Note NCAR/TN-398+IA, 107 pp. [Available from NCAR, P.O. Box 3000, Boulder, CO 80307.]
- Gruber, A., and A. F. Krueger, 1984: The status of the NOAA outgoing longwave radiation data set. *Bull. Amer. Meteor. Soc.*, **65**, 958–962.
- Gutman, G., and W. S. Schwerdtfeger, 1965: The role of latent and sensible heat for the development of a high pressure system over the subtropical Andes, in summer. *Meteor. Rundsch.*, **17**, 1–7.
- Holton, J. R., 1992: *An Introduction to Dynamic Meteorology*. 3d ed. Academic Press, 512 pp.
- Horel, J., A. Nahmann, and J. Geisler, 1989: An investigation of the annual cycle of the convective activity over the tropical Americas. *J. Climate*, **2**, 1388–1403.
- Houze, R. A., 1993: *Cloud Dynamics*. 1st ed. Academic Press, 573 pp.
- Hsie, E.-Y., R. A. Anthes, and D. Keyser, 1984: Numerical simulation of frontogenesis in a moist atmosphere. *J. Atmos. Sci.*, **41**, 2581–2594.
- Jones, C., 1990: An investigation of low-frequency variability of the large-scale circulation over South America. M.S. thesis, University of Utah, 103 pp. [Available from Meteorology Department, University of Utah, Salt Lake City, UT 84112-0110.]
- Kain, J. S., and J. M. Fritsch, 1993: Convective parameterization for mesoscale models: The Kain–Fritsch scheme. *The Representation of Cumulus Convection in Numerical Models*, Meteor. Monogr., No. 46, Amer. Meteor. Soc., 165–170.
- Kalnay, E., and Coauthors, 1996: The NCEP/NCAR 40-Year Reanalysis Project. *Bull. Amer. Meteor. Soc.*, **77**, 437–472.
- Kiladis, G. N., and K. M. Weickmann, 1997: Horizontal structure and seasonality of large-scale circulations associated with sub-monthly tropical convection. *Mon. Wea. Rev.*, **125**, 1997–2013.
- Legates, P., and H. Willmont, 1990: A climatology of global precipitation. *Int. J. Climatol.*, **10**, 111–127.
- Lenters, J. D., and K. H. Cook, 1995: Simulation and diagnosis of the regional summertime precipitation climatology of South America. *J. Climate*, **8**, 2298–3005.
- , and —, 1997: On the origin of the Bolivian high and related circulation features of the South American climate. *J. Atmos. Sci.*, **54**, 656–677.
- , and —, 1999: Summertime precipitation variability over South America: Role of the large-scale circulation. *Mon. Wea. Rev.*, **127**, 409–431.
- Mo, K. C., and R. W. Higgins, 1997: The Pacific South American modes and tropical convection during the Southern Hemisphere winter. *Mon. Wea. Rev.*, **126**, 1581–1596.
- Negri, A., R. Adler, R. Maddox, K. Howard, and P. Keehn, 1993: A regional rainfall climatology over Mexico and the southwest United States derived from passive microwave and geosynchronous infrared data. *J. Climate*, **6**, 2144–2161.
- Nogues-Paegle, J., and K. C. Mo, 1997: Alternating wet and dry conditions over South America during summer. *Mon. Wea. Rev.*, **125**, 279–291.
- Orlanski, I., 1975: A rational subdivision of scale for atmospheric processes. *Bull. Amer. Meteor. Soc.*, **56**, 527–530.
- Rao, G. V., and S. Erdogan, 1989: The atmospheric heat source over

- the Bolivian Plateau for a mean January. *Bound.-Layer Meteor.*, **46**, 13–33.
- Rossow, W., and R. Schiffer, 1991: ISCCP cloud data products. *Bull. Amer. Meteor. Soc.*, **72**, 2–20.
- Schwerdtfeger, W., 1976: High thunderstorm frequency over the subtropical Andes during the summer: Cause and effects. *Climate of Central and South America*, W. Schwerdtfeger, Ed., Elsevier, 192–195.
- Stull, R. B., 1989: *An Introduction to Boundary Layer Meteorology*. 2d ed. Kluwer Academic Publishers, 665 pp.
- Tang, M., and E. R. Reiter, 1984: Plateau monsoons of the Northern Hemisphere: A comparison between North America and Tibet. *Mon. Wea. Rev.*, **112**, 617–629.
- Thompson, L. G., E. Mosley-Thompson, and B. Morales, 1984: El Niño–Southern Oscillation events recorded in stratigraphy of the tropical Quelccaya Ice Cap, Peru. *Science*, **226**, 50–53.
- Tripoli, G. J., and W. R. Cotton, 1989: Numerical study of an observed orogenic mesoscale convective system. Part I: Simulated genesis and comparison with observations. *Mon. Wea. Rev.*, **117**, 273–304.
- Virji, H., 1981: A preliminary study of summertime tropospheric circulation patterns over South America estimated from cloud winds. *Mon. Wea. Rev.*, **109**, 599–612.
- Vuille, M., D. R. Hardy, C. Braun, F. Keimig, and R. S. Bradley, 1998: Atmospheric circulation anomalies associated with 1996/97 summer precipitation events on Sajama Ice Cap, Bolivia. *J. Geophys. Res.*, **103**, 11 191–11 204.
- Wang, W., and N. L. Seaman, 1997: A comparison study of convective parameterization schemes in a mesoscale model. *Mon. Wea. Rev.*, **125**, 252–278.
- Wolyn, P. G., and T. B. McKee, 1994: The mountain–plains circulation east of a 2-km-high north–south barrier. *Mon. Wea. Rev.*, **122**, 1490–1508.
- Zhou, J., and K. M. Lau, 1998: Does a monsoon climate exist over South America? *J. Climate*, **11**, 1020–1040.